NuSTAR HARD X-RAY SURVEY OF THE GALACTIC CENTER REGION. I. HARD X-RAY MORPHOLOGY AND SPECTROSCOPY OF THE DIFFUSE EMISSION

KAYA MORI[1], CHARLES J. HAILEY[1], ROMAN KRIVONOS[2,3], JAESUB HONG[4], GABRIELE PONTI[5], FRANZ BAUER[6,7,8], KERSTIN PEREZ[1,9], MELANIA NYNKA[1], SHUO ZHANG[1], JOHN A. TOMSICK[2], DAVID M. ALEXANDER[10], FREDERICK K. BAGANOFF[11], DIDIER BARRET[12,13], NICOLAS BARRIÈRE[2], STEVEN E. BOGGS[2], ALICIA M. CANIPE[1], FINN E. CHRISTENSEN[14], WILLIAM W. CRAIG[2,15], KARL FORSTER[16], PAOLO GIOMMI[17], BRIAN W. GREFENSTETTE[16], JONATHAN E. GRINDLAY[4], FIONA A. HARRISON[16], ALLAN HORNSTRUP[14], TAKAO KITAGUCHI[18,19], JASON E. KOGLIN[20], VY LUU[1], KRISTEN K. MADSEN[16], PETER H. MAO[16], HIROMASA MIYASAKA[16], MATTEO PERRI[17,21], MICHAEL J. PIVOVAROFF[15], SIMONETTA PUCCETTI[17,21], VIKRAM RANA[16], DANIEL STERN[22], NIELS J. WESTERGAARD[14], WILLIAM W. ZHANG[23], AND ANDREAS ZOGLAUER[2]

[1] Columbia Astrophysics Laboratory, Columbia University, New York, NY 10027, USA; kaya@astro.columbia.edu
[2] Space Sciences Laboratory, University of California, Berkeley, CA 94720, USA
[3] Space Research Institute, Russian Academy of Sciences, Profsoyuznaya 84/32, 117997 Moscow, Russia
[4] Harvard-Smithsonian Center for Astrophysics, Cambridge, MA 02138, USA
[5] Max-Planck-Institut f. extraterrestrische Physik, HEG, Garching, Germany
[6] Instituto de Astrofísica, Facultad de Física, Pontificia Universidad Católica de Chile, 306, Santiago 22, Chile
[7] Millennium Institute of Astrophysics, Santiago, Chile
[8] Space Science Institute, 4750 Walnut Street, Suite 205, Boulder, Colorado 80301, USA
[9] Haverford College, 370 Lancaster Avenue, KINSC L109, Haverford, PA 19041, USA
[10] Department of Physics, Durham University, Durham DH1 3LE, UK
[11] Kavli Institute for Astrophysics and Space Research, Massachusets Institute of Technology, Cambridge, MA 02139, USA
[12] Université de Toulouse, UPS-OMP, IRAP, Toulouse, France
[13] CNRS, Institut de Recherche en Astrophysique et Planétologie, 9Av. colonel Roche, BP 44346, F-31028 Toulouse Cedex 4, France
[14] DTU Space—National Space Institute, Technical University of Denmark, Elektrovej 327, DK-2800 Lyngby, Denmark
[15] Lawrence Livermore National Laboratory, Livermore, CA 94550, USA
[16] Cahill Center for Astronomy and Astrophysics, California Institute of Technology, Pasadena, CA 91125, USA
[17] ASI Science Data Center, Via del Politecnico snc I-00133, Roma, Italy
[18] Department of Physical Science, Hiroshima University, Higashi-Hiroshima, Hiroshima 739-8526, Japan
[19] Core of Research for the Energetic Universe, Hiroshima University, Higashi-Hiroshima, Hiroshima 739-8526, Japan
[20] Kavli Institute for Particle Astrophysics and Cosmology, SLAC National Accelerator Laboratory, Menlo Park, CA 94025, USA
[21] INAF—Astronomico di Roma, via di Frascati 33, I-00040 Monteporzio, Italy
[22] Jet Propulsion Laboratory, California Institute of Technology, Pasadena, CA 91109, USA
[23] NASA Goddard Space Flight Center, Greenbelt, MD 20771, USA

ABSTRACT

We present the first sub-arcminute images of the Galactic Center above 10 keV, obtained with *NuSTAR*. *NuSTAR* resolves the hard X-ray source IGR J17456–2901 into non-thermal X-ray filaments, molecular clouds, point sources, and a previously unknown central component of hard X-ray emission (CHXE). *NuSTAR* detects four non-thermal X-ray filaments, extending the detection of their power-law spectra with $\Gamma \sim 1.3$–2.3 up to ~50 keV. A morphological and spectral study of the filaments suggests that their origin may be heterogeneous, where previous studies suggested a common origin in young pulsar wind nebulae (PWNe). *NuSTAR* detects non-thermal X-ray continuum emission spatially correlated with the 6.4 keV Fe Kα fluorescence line emission associated with two Sgr A molecular clouds: MC1 and the Bridge. Broadband X-ray spectral analysis with a Monte-Carlo based X-ray reflection model self-consistently determined their intrinsic column density ($\sim 10^{23}\,\mathrm{cm}^{-2}$), primary X-ray spectra (power-laws with $\Gamma \sim 2$) and set a lower limit of the X-ray luminosity of Sgr A* flare illuminating the Sgr A clouds to $L_X \gtrsim 10^{38}\,\mathrm{erg\,s}^{-1}$. Above ~20 keV, hard X-ray emission in the central 10 pc region around Sgr A* consists of the candidate PWN G359.95–0.04 and the CHXE, possibly resulting from an unresolved population of massive CVs with white dwarf masses $M_{\mathrm{WD}} \sim 0.9\,M_\odot$. Spectral energy distribution analysis suggests that G359.95–0.04 is likely the hard X-ray counterpart of the ultra-high gamma-ray source HESS J1745–290, strongly favoring a leptonic origin of the GC TeV emission.

Key words: Galaxy: center – radiation mechanisms: non-thermal – X-rays: general – X-rays: ISM

1. INTRODUCTION

The relative proximity of the Galactic Center (GC), at ~8 kpc, allows for sensitive, high-resolution observations that are not possible for more distant galactic nuclei. Over the last two decades, the GC and Galactic Ridge have been extensively surveyed by X-ray telescopes, which have revealed various diffuse X-ray components including the Galactic Ridge X-ray emission (GRXE; Revnivtsev et al. 2006; Krivonos et al. 2007; Yuasa et al. 2012), an X-ray haze that extends out from the GC

for ~60° in longitude and a few degrees in latitude (Worrall et al. 1982), and large-scale diffuse Fe line emission (Koyama et al. 1989, 1996). In the inner 20′ around the GC, a separate, unresolved ~8 keV thermal component has been observed by *Chandra* and *XMM-Newton* (Muno et al. 2004; Heard & Warwick 2013). *Chandra* has resolved thousands of point sources in the $2° \times 0°.8$ GC field, suggesting the $kT \sim 8$ keV thermal emission represents a population of unresolved magnetic CVs (Wang et al. 2002a; Muno et al. 2009;

Revnivtsev et al. 2009). In addition, *Chandra* has performed arcsecond-scale mapping in the crowded soft X-ray (2–10 keV) band (Baganoff et al. 2003), identifying emission from the central supermassive black hole Sgr A*, hot gas from winds of the surrounding central stellar cluster, the supernova remnant (SNR) Sgr A East, non-thermal filamentary structures, molecular clouds and thousands of X-ray point sources (Muno et al. 2008).

In the GC region, *Chandra* has detected nearly two dozen X-ray filaments, most of which exhibit "cometary" or "filamentary" shapes and featureless non-thermal spectra with $\Gamma \sim 1.5$–2.5 (Johnson et al. 2009). Muno et al. (2008) and Lu et al. (2008) speculated that the X-ray filaments are young pulsar wind nebulae (PWNe) since they possess similar spectral and morphological properties, although there is as yet no direct evidence for a PWN. Whether X-ray filaments are PWNe or not, if synchrotron radiation is responsible for their non-thermal X-ray emission, hard X-ray spectroscopy probes the highest energy ($\sim$10–100 TeV) electrons that are accelerated since the synchrotron photon energy $E_\gamma \sim 40$ $(E_e/10 \, \text{TeV})^2$ $(B/1 \, \text{mG})$ keV where E_e is the electron energy and B is the magnetic field strength typically $\sim$0.1–1 mG inside radio filaments (Yusef-Zadeh & Morris 1987; Ferrière 2009).

Many of the Galactic Center molecular clouds (GCMCs) in the Sgr A, B, and C regions are known to produce diffuse Fe Kα fluorescence emission at 6.4 keV (Ponti et al. 2014). Two models, the so-called X-ray reflection nebula (XRN) model (Sunyaev et al. 1993) and the low-energy cosmic-ray (LECR) model (Yusef-Zadeh et al. 2002a), have been proposed to account for Fe Kα line emission by photo-ionization by an external X-ray source and collisional ionization by LECR, repectively (see Ponti et al. 2013, for a review). The XRN scenario seems more plausible since the *XMM-Newton* and *Chandra* surveys of the GC region over the last decade have revealed the year-scale time variation of strong Fe Kα line with EW $\sim$1 keV in the Sgr A clouds (Ponti et al. 2010; Capelli et al. 2012; Clavel et al. 2013) and Sgr B2 (Terrier et al. 2010). It has been proposed that the X-ray emission of GCMCs is associated with Sgr A* past flares, or nearby X-ray transients (Sunyaev et al. 1993; Koyama et al. 1996). However, it is still possible that the LECR emission contributes as an additional component given that a large population of cosmic rays are expected in the GC (Capelli et al. 2012). In either case, there has been no clear detection of X-ray continuum emission intrinsic to the Sgr A clouds. In the soft X-ray band, thermal diffuse emission as well as point sources heavily contaminate X-ray emission from the Sgr A clouds, while hard X-ray telescopes such as *INTEGRAL* were not able to resolve X-ray continuum emission from the Sgr A clouds.

In the gamma-ray band, the CANGAROO-II and HESS arrays of Cherenkov telescopes discovered the ultra-high energy gamma-ray source HESS J1745–290 (Aharonian et al. 2004; Tsuchiya et al. 2004) and later its 0.1–10 TeV spectrum was well measured by different TeV telescopes such as HESS (Aharonian et al. 2009), VERITAS (Archer et al. 2014) and MAGIC (Albert et al. 2006). Both Sgr A* and the cometary PWN candidate G359.95–0.04 have been proposed as counterparts of the TeV source HESS J1745–290, as both lie within its 13″ error radius (Acero et al. 2010). This has led to two possible interpretations: a leptonic and a hadronic origin. In the leptonic scenario, high-energy electrons are accelerated by Sgr A* flares, PWNe, SNRs interacting with molecular clouds and stellar winds. These TeV electrons emit synchrotron radiation in the X-ray band in an ambient interstellar medium (ISM) magnetic field of $\sim$10 μG and also emit inverse-Compton radiation in the gamma-ray band by up-scattering ultraviolet and far-infrared photons in the high radiation density field of the GC (Hinton & Aharonian 2007). In the hadronic scenario, relativistic protons accelerated from Sgr A* or SNRs interacting with the surrounding medium emit gamma-rays via pion decay, then secondary electrons emit X-rays via synchrotron or non-thermal bremsstrahlung radiation (Chernyakova et al. 2011). Both hadronic and leptonic models can also explain the 0.1–10 TeV spectrum of the GC, either via pion decay from protons injected into the diffuse ISM by past Sgr A* outflows (Aharonian & Neronov 2005; Ballantyne et al. 2007; Chernyakova et al. 2011) or via inverse-Compton emission from a population of electrons ejected from Sgr A* (Kusunose & Takahara 2012) or the PWN candidate G359.95–0.04 (Hinton & Aharonian 2007). As a more exotic scenario, dark matter annihilation at the GC has been also proposed (Cembranos et al. 2013). Since the soft X-ray emission of the GC is dominated by diffuse thermal emission and point sources that are mostly unrelated to the GeV to TeV emission, it is extremely important to identify a hard X-ray counterpart of HESS J1745–290. However, the central 10 pc region of the GC has been difficult to localize due to the $\gtrsim$10′ angular resolution of hard X-ray instruments (Winkler et al. 2003; Gehrels et al. 2004), leaving the origin and nature of HESS J1745–290 a subject of controversy.

Above 20 keV, the *INTEGRAL* observatory discovered a persistent hard X-ray source IGR J17456–2901, which is particularly bright in the 20–40 keV range, within 1′ of the GC (Bélanger et al. 2006). The emission at energies above 40 keV, however, seems to shift several arcminutes to the east of both Sgr A* and Sgr A East. This variation in the position of the emission combined with the 12′ spatial resolution of the *INTEGRAL*/IBIS coded aperture mask has led to speculation that the emission results not from a single object, but from a collection of the many surrounding diffuse and point-like X-ray sources (Krivonos et al. 2007). However, without high-resolution, high-energy images of the region available, the existence of a new source of high-energy X-ray emission could not be ruled out.

The *NuSTAR* hard X-ray telescope (Harrison et al. 2013), with its arcminute angular resolution and effective area extending from 3 to 79 keV, can make unique contributions to understanding the emission mechanisms of X-ray filaments, GCMCs and the gamma-ray source HESS J1745–290. Broadband X-ray spectroscopy with *NuSTAR* provides a powerful diagnostic that can distinguish between different models of GCMC X-ray emission and tightly constrain parameters when combined with self-consistent X-ray emission models. In addition, *NuSTAR* is the key to filling the gap between the well-studied soft X-ray populations and the persistent gamma-ray emission in the central parsec region of the GC.

In this paper, we report *NuSTAR* hard X-ray observations of diffuse emission in the GC region, while our companion paper (Hong et al. 2015) focuses on the hard X-ray point sources. Section 2 outlines the *NuSTAR* and *XMM-Newton* observations adopted for studying GC diffuse emission, followed by Section 3 describing our imaging and spectral analysis methods. Section 4 presents the hard X-ray morphology of the GC region above 10 keV. For three hard X-ray diffuse

Table 1
NuSTAR and *XMM-Newton* Galactic Center Observations in 2012

ObsID	Start Date (UTC)	Exposure (ks)	Target
NuSTAR			
30001002001	2012 Jul 20	166.2	Sgr A*
30001002003	2012 Aug 04	83.8	Sgr A*
30001002004	2012 Oct 16	53.6	Sgr A*
40010001002	2012 Oct 13	23.9	Mini-survey
40010002001	2012 Oct 13	24.2	Mini-survey
40010003001	2012 Oct 14	24.0	Mini-survey
40010004001	2012 Oct 15	24.0	Mini-survey
40010005001	2012 Oct 15	25.7	Mini-survey
40010006001	2012 Oct 16	23.5	Mini-survey
XMM-Newton[a]			
0694640301	2012 Aug 31	35.5	CMZ[b]
0694640401	2012 Sep 02	43.9	CMZ[b]
0694641001	2012 Sep 23	40.7	CMZ[b]
0694641101	2012 Sep 24	35.5	CMZ[b]

Notes. The exposure times listed are corrected for good time intervals.
[a] All *XMM-Newton* observations were operated in Full Frame mode with the medium filter.
[b] Central Molecular Zone.

source categories, namely non-thermal X-ray filaments (Section 5), molecular clouds (Section 6) and the central 10 parsec region around Sgr A* (Section 7), we present our *NuSTAR* spectral and morphological analysis jointly with archived *Chandra* and *XMM-Newton* data, and discuss implications for their hard X-ray emission mechanisms. Section 8 summarizes our results from the *NuSTAR* GC survey. The Appendix describes *NuSTAR* background components and background subtraction methods, some of which are peculiar to the *NuSTAR* GC observations, as well as X-ray reflection models for GCMCs particularly on a Monte-Carlo based self-consistent MYTorus model. Throughout the paper, we assume a distance to the GC of 8 kpc (Reid 1993).

2. *NuSTAR* OBSERVATIONS

NuSTAR consists of coaligned X-ray telescopes with corresponding focal plane modules (FPMA and FPMB) with an angular resolution of 58″ Half Power Diameter (HPD) and 18″ Full Width Half Maximum (FWHM; Harrison et al. 2013). *NuSTAR* operates in the 3–79 keV band with ~400 eV (FWHM) energy resolution below ~50 keV and ~900 eV at 68 keV. Soon after its launch in 2012 June, *NuSTAR* initiated a large GC survey to study both point sources and diffuse emission in the hard X-ray band. A number of single pointing observations, occasionally coordinated with other telescopes, were performed to study Sgr A* flaring (Barrière et al. 2014), the newly discovered magnetar SGR 1745–29 (Mori et al. 2013; Kaspi et al. 2014), the Cannonball (Nynka et al. 2013), Sgr A-E (Zhang et al. 2014), X-ray transients in outbursts (Koch et al. 2014; Barrière et al. 2015), the Arches cluster (Krivonos et al. 2014) and Sgr B2 molecular cloud (Zhang et al. 2015).

For the analysis of GC diffuse emission presented in this paper, we used the nine *NuSTAR* observations listed in Table 1.

The first three observations were pointed at Sgr A*, while the next six observations, each with ~25 ks depth, covered the ~0°.4 × 0°.3 area between Sgr A* and the low mass X-ray binary (LMXB) 1E1743.1–2843 (hereafter referred to as the "mini-survey"). The *NuSTAR* mini-survey was originally motivated to study the *INTEGRAL* source IGR J17456–2901. We did not use *NuSTAR* observations of Sgr A* in 2013 and 2014 since the data were heavily contaminated by outbursting X-ray transients. The other observations surveying larger regions, ≳10′ away from the GC, were primarily aimed at studying point sources, and so they are not included in this analysis. In addition, four *XMM-Newton* observations in 2012 (Table 1) were obtained in the Full Frame mode with the medium filter and their data are used for joint spectral analysis.

3. DATA REDUCTION AND ANALYSIS

In this section, we describe our imaging and spectral analysis of the *NuSTAR* GC data. All the *NuSTAR* data were processed using the *NuSTAR Data Analysis Software* (*NuSTARDAS*) v1.3.1. After filtering high background intervals during South Atlantic Anomaly (SAA) passages, we removed additional time periods in which Sgr A* was in a flaring state, as observed by *NuSTAR* or during coincident *Chandra* observations (Barrière et al. 2014). An additional 70 ks was removed from the 2012 August observation (ObsID: 30001002003) due to a reduction in the event rate of FPMA, possibly due to debris blocking the detector. After all quality cuts, the effective exposure time ranges from ~25 to 100 ks (mini-survey) to ~300 ks (Sgr A*) (Table 1 and Figure 1).

In most *NuSTAR* GC observations, the background below ~40 keV is dominated by photons from outside the field of view (FOV) entering through the aperture stop (so-called "stray-light background" or SLB hereafter Harrison et al. 2013; Krivonos et al. 2014; Wik et al. 2014). In particular, SLB patterns from nearby bright point sources ($\gtrsim 10^{-11}$ erg cm^{-2} s^{-1}) within ~5° from the telescope's pointing vector are visible at predictable locations on the FOV and completely dominate over other X-ray emission. We filtered out events in the region of heavy SLB contamination from the nearby bright source GX 3 +1 (Seifina & Titarchuk (2012) see the Appendix for more details). As a result, ~25% of FPMB events, mostly in detector chip 0, were removed from all observations, while FPMA data do not have significant SLB from bright point sources.

3.1. Imaging Analysis

First, we applied astrometric corrections for individual *NuSTAR* event files by registering known soft X-ray sources to further improve our positioning accuracy for detailed morphological studies. These registration sources include bright *Chandra* point sources (Muno et al. 2009), the core of the Sgr A-E (Sakano et al. 2003), the Arches cluster (Yusef-Zadeh et al. 2002b) and the Cannonball (a neutron star candidate located outside the Sgr A East shell) (Park et al. 2005; Nynka et al. 2013). They all have *Chandra* counterparts with known positions to better than ~0″.5. Using the IDL centroiding routine gcntrd, we determined the centroid of each registration source in the 3–10 keV band, matching *Chandra*'s sensitive energy band (2–8 keV) for highly absorbed GC sources. Two of the Sgr A* observations (ObsID: 30001002001, 30001002004) contained several bright
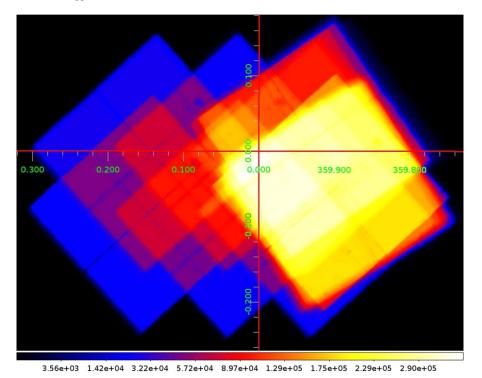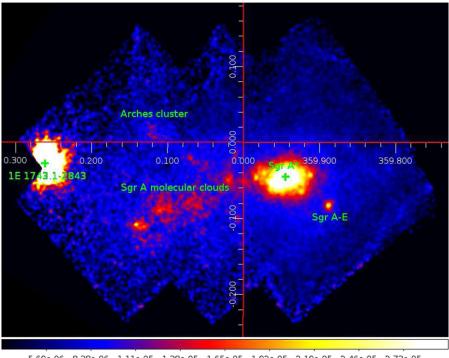
Figure 1. Exposure map of the nine *NuSTAR* observations of the GC region combined before removing the high stray-light background regions contaminated by nearby bright point sources. Exposure time in seconds is plotted in the square root scale in the Galactic coordinates [°].

Figure 2. *NuSTAR* 10–79 keV exposure-corrected smoothed image of the GC in the Galactic coordinates [°]. The image was smoothed by a 5-pixel (12″3) Gaussian kernel. The image scaling was adjusted to illustrate the X-ray features clearly.

flares from Sgr A* itself (Barrière et al. 2014) that aided in determining the astrometric corrections. For these two observations, an image file was created that contained the bright flares from Sgr A* and we defined the offset as the difference between the radio position of Sgr A* (Reid et al. 1999) and the centroid of the *NuSTAR* emission. These event files, after removing Sgr A* flare intervals, were properly shifted using the Sgr A* flare position and used in the subsequent mosaic images presented here. Translational shifts by as much as ~14″ were required to place the target source at its known position, and were applied to both event files and exposure maps.

Second, after each observation was corrected for its offset, we summed together all observations and normalized the resulting image by the effective exposure map. We neither subtracted background nor corrected for vignetting effects (so-called flat-fielding) in the subsequent imaging analysis since the background is not spatially uniform (see Appendix). Figure 2 shows the exposure-corrected count rate images in the 10–79 keV band, after combining both FPMA and FPMB data from the nine *NuSTAR* observations. For illustration purposes, we smoothed *NuSTAR* images with a Gaussian kernel of radius $\sim 12''$ (5 pixels) unless otherwise instructed. We verified the applied astrometric correction by determining the position of one or several additional sources in each individual observation and in the final mosaicked image. The *NuSTAR* positions are within $5''$ of the reported *Chandra* positions.

There are two particularly bright regions seen in the *NuSTAR* images. One of them is the Sgr A complex containing thermal diffuse emission, hundreds of X-ray point sources, X-ray filaments and thermal emission from Sgr A East. Although these X-ray sources are unresolved by *NuSTAR* in the 3–10 keV band, most of them have soft X-ray spectra and fade out beyond 10 keV making a subset of X-ray sources more prominent (Section 4). The other bright region near the left (east) side of the image is a persistent LMXB 1E1743.1−2843 at R.A. $= 17^{\rm h}46^{\rm m}21\overset{s}{.}094$ and decl. $= -28°$ $43'42''.3$ (J2000.0 Wijnands et al. 2006). The LMXB looks "extended" because it is so bright, with a 3–79 keV flux of 2.2×10^{-10} erg cm^{-2} s^{-1} (Lotti et al. 2015), that its point-spread function (PSF) wings extending beyond $\sim 1'$ are still dominant over other X-ray emission. Ghost-ray background (see its definition in the Appendix) from 1E1743.1−2843 is not visible, and our simulation confirmed that it is below the GC diffuse emission and SLB in most of the area covered by the *NuSTAR* mini-survey observations. The brightest X-ray filament is Sgr A-E (G359.89–0.08) at R.A. $= 17^{\rm h}45^{\rm m}40\overset{s}{.}4$ and decl. $= -29°04'29''.0$ (J2000.0 Lu et al. 2003) and it is distinct from the Sgr A* complex. The molecular clouds in the region between the Sgr A* complex and 1E1743.1−2843 (Ponti et al. 2010) are also visible. The outer regions at $b \gtrsim 0°.1$ or $b \lesssim 0°.2$ are dominated by SLB from the GRXE, and no GC emission is clearly visible there.

3.2. Trial Probability Map

In addition to the exposure-corrected images, we present a sky map of detection significance, dubbed a "trial map," to illustrate detection significance of faint sources that are otherwise hidden in the count rate images (see Hong et al. (2015) for more details and applications to *NuSTAR* images). The value of the trial map at each sky position represents the number of random trials required to produce the observed counts by purely random Poisson fluctuations if no excess of X-ray sources relative to the background is present at the location. For every sky position, we first define a source cell (e.g., 20% encircled energy fraction of the PSF) and a background cell (an annulus around the position), and then, using the cells, we calculate the total observed counts (S) and their background counts (λ_B). For each image pixel, the random trial number is estimated to be a normalized incomplete gamma function of S and λ_B (Weisskopf et al. 2007; Kashyap et al. 2010). We repeat the procedure for other pixels to generate the map by sliding cell windows across the field.

Throughout the paper, the negative logarithm of the trial probability is plotted in the trial map [e.g., $-\log(10^{-6}) = 6$ for a trial probability of $P_{\rm trial} = 10^{-6}$]. Thus, a brighter spot indicates higher detection significance. When there are no significant systematic fluctuations, the presence of an X-ray source is indicated by a position where the trial probability is significantly smaller than the odds one can reach with the total number of independent searches (i.e., the inverse of the total number of searches). The total number of independent searches can be estimated as the maximal number of resolvable sources (N_R) in the field, which is the ratio of the number of pixels in the image ($N_P = 1.7 \times 10^5$ pixels in this example presented in Section 4.3) to the *NuSTAR* angular resolution in pixels (FWHM $\sim 18''$ diameter circle: ~ 40 pixels). For a given confidence level (C), one can claim a detection when $P_{\rm trial} < N_R * (1 - C)$. For instance, to detect a source at 99.7% confidence level (i.e., 3σ detection), $P_{\rm trial}$ should be less than $10^{-6.1}$ or its trial map value should be greater than 6.1. Similarly for 4 and 5σ detections, the trial map value should be greater than 7.8 and 9.9, respectively. Note that trial maps are not used to infer the actual source brightness and they are presented without any smoothing.

3.3. Spectral Analysis

For some of the hard X-ray sources discussed below, we have jointly analyzed the *NuSTAR* and *XMM-Newton* spectra to investigate their X-ray emission mechanisms by comparing with several existing models. We extracted *NuSTAR* source spectra and generated response matrices and ancillary files using *nuproducts*. Background subtraction and modeling require extra caution due to the high background level and to its complex multiple components (Appendix). Background substraction methods are specific to each source and they can be found in later sections (e.g., Sections 6.1 and 7.1) where we clarify our data selection and filtering.

We processed all the *XMM-Newton* Observation Data Files with the *XMM-Newton* Science Analysis System (SAS version 13.5.0) and the most recent calibration files. We restricted our analysis to the *XMM-Newton* EPIC-PN data where photon pile-up effect is negligible for the sources we analyzed. After filtering out time intervals with high soft proton flaring levels, we selected EPIC-PN events with FLAG = 0 and PATTERN $\leqslant$ 4. For each *XMM-Newton* spectrum, the response matrix and effective area files are computed with the XMM-SAS tasks `rmfgen` and `arfgen`. For the background, we adopted the *XMM-Newton* calibration observations closest in time to each of the *XMM-Newton* observations, and used their EPIC-PN data with the filter wheel closed (FWC), thus blocking external X-rays and soft protons, and allowing us to measure internal background components accurately. First, we fit the so-called FWC spectra with several power-law continuum components and Gaussian lines to properly parameterize the background emission. Since the ratio between the lines and continuum in background spectra is stable between observations close in time, we scaled the overall normalization of the FWC model to match the count rates from the same source-free region between the FWC model and actual *XMM-Newton* science data, while we froze all the other parameters.

We combined *NuSTAR* FPMA and FPMB spectra and response files using the FTOOL *addascaspec*. *XMM-Newton* EPIC-PN spectra and response files from individual
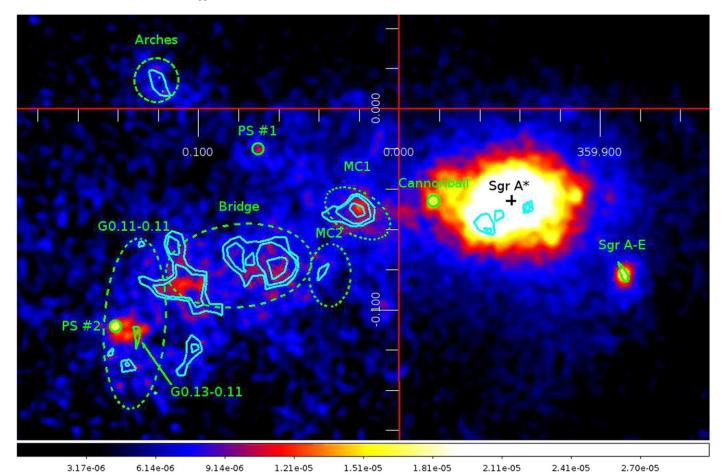
Figure 3. *NuSTAR* 10–20 keV exposure-corrected smoothed image of the GC region in the Galactic coordinates [°]. Green dashed ellipses: selected molecular clouds. Cyan contours: 6.4 keV Fe K-α continuum-subtracted intensity contours from *XMM-Newton*. Green polygons: *Chandra* morphologies of the two X-ray filaments detected above 10 keV. Green circles ($r = 10''$): two hard X-ray point sources. PS #1 and #2 are known *Chandra* point sources, CXOUGC J174551.9–285311 and CXOUGC J174622.7–285218, respectively (Muno et al. 2009).

observations were similarly combined, after ensuring that individual spectra were consistent with each other. We grouped all spectra so that each bin had sufficient counts to ensure that it had a significance over background of at least 4σ. All spectral fitting and flux derivations were performed in XSPEC (Arnaud 1996), with photoionization cross sections as defined in Verner et al. (1996) and abundances for the interstellar absorption as defined in Wilms et al. (2000). Chi-squared statistics were used for spectral fitting, and all quoted errors are for 1σ level confidence.

4. HARD X-RAY MORPHOLOGY OF THE GC REGION

4.1. 10–20 keV Band Morphology

Figure 3 shows the *NuSTAR* image in the 10–20 keV band. Some features are identified as point sources and marked with white circles (Hong et al. 2015). While 8 keV thermal emission and SNR Sgr A East emission are still dominant, the Cannonball (Nynka et al. 2013) is visible in the 10–20 keV image. Diffuse emission is present in the region east of the Sgr A* complex but west of the LMXB 1E1743.1–2843. This diffuse emission is likely a mixture of 8 keV thermal emission and molecular cloud X-ray continuum. Three molecular clouds, namely MC1, the Bridge and the Arches cluster indicated by green dashed ellipses (defined in Ponti et al. 2010), are clearly detected above 10 keV, while we do not detect diffuse emission

from these clouds above 20 keV largely due to the high background level. The *NuSTAR* image is overlaid with Fe Kα line intensity contours obtained from the 2012 *XMM-Newton* observations (cyan contours). The continuum emission in the 4.5–6.28 keV band was subtracted from the 6.28–6.53 keV *XMM-Newton* image to emphasize just the Fe Kα line emission (Ponti et al. 2010). The 10–20 keV hard X-ray emission is well correlated with the Fe Kα line contours in these cloud regions.

With a separation of $\sim 5'$, MC1 is the closest to Sgr A* in projection among the molecular clouds emitting the Fe Kα line. MC1 was one of the brightest clouds in 2012, and the Fe Kα line flux of the overall cloud stayed nearly constant from 2000 to 2010 (Ponti et al. 2010; Capelli et al. 2012). The bright 10–20 keV emission in MC1 coincides with the strong Fe Kα line emission seen in 2012. Using *Chandra* data, Clavel et al. (2013) found different time variations in sub-divided regions in the MC1 cloud between 2000 and 2010—the Fe Kα line flux decreased in the two regions dubbed "a" and "b" while it increased in the four regions dubbed "c" to "f" in Figure 4. In 2012, *XMM-Newton* and *NuSTAR* detected the brightest Fe Kα line and hard X-ray continuum emission coinciding with the "c" region, where Fe Kα line flux has been most prominent in MC1 since 2002 (Clavel et al. 2013).

The so-called Bridge is located on the east side of MC1. It contains multiple clouds exhibiting a range of Fe Kα line flux light curves (Ponti et al. 2010; Capelli et al. 2012; Clavel
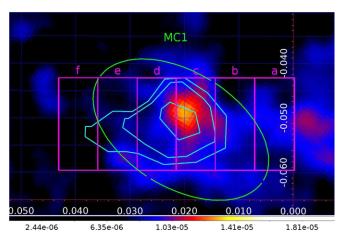
Figure 4. *NuSTAR* 10–20 keV image zoomed around MC1 cloud region in the Galactic coordinates [°] overlaid with a region used for extracting *XMM-Newton* and *NuSTAR* spectra of MC1 (green), Fe Kα line intensity contours from 2012 *XMM-Newton* observations (cyan), and the six $26'' \times 61''$ rectangular subregions (magenta) defined in Clavel et al. (2013).

et al. 2013). In the Bridge, there are two bright regions both in the Fe Kα line and hard X-ray continuum emission. They correspond to the two distinct regions observed in the N_2H^+ map at molecular line velocity $\sim +50$ km s^{-1} (Jones et al. 2012), dubbed the Br1 and Br2 regions by Clavel et al. (2013). Spectral analysis of MC1 and the Bridge is presented in Section 6, while detailed imaging and spectral analysis of the Arches cluster can be found in Krivonos et al. (2014).

The east end of the Bridge is another molecular cloud, located at G0.11–0.11. In G0.11–0.11, there are two hard X-ray sources that do not emit a strong Fe Kα line at 6.4 keV. One is the X-ray filament G0.13–0.11 (Section 5.3), while the other is the bright magnetic CV CXOUGC J174622.7–285218 (Muno et al. 2009). Unlike the GCMC, these two sources do not have strong Fe Kα line emission and thus do not appear in the 6.4 keV Fe Kα contours. Otherwise, we detected neither strong Fe Kα nor hard X-ray continuum emission associated with the molecular cloud in G0.11–0.11 probably because its X-ray flux has been decaying over the last decade (Capelli et al. 2012). No hard X-ray emission above 10 keV was detected from other clouds such as MC2, the 20 and 50 km s^{-1} clouds. Continuing the linearly decreasing trend of Fe Kα line flux (Clavel et al. 2013), hard X-ray emission from MC2 may have slipped below the *NuSTAR* detection threshold. Our results are consistent with no apparent detection of Fe Kα emission from the 20 km s^{-1} cloud and the 50 km s^{-1} cloud (Ponti et al. 2010). However, given their small offsets ($\lesssim$10 pc) relative to the GC where X-ray transients are highly concentrated (Muno et al. 2005), X-ray outbursts lasting over a few years (e.g., SGR J1745–29) may illuminate these clouds, and thus X-ray reflection from there may be observed through time-varying Fe Kα line and hard X-ray continuum emission in the near future.

4.2. 20–40 keV Band Morphology

Above 20 keV, besides the LMXB 1E1743.1–2843 and Sgr A-E, hard X-ray emission is observed within a $\sim 3'$ radius region around Sgr A*. In order to investigate the central emission morphology precisely while avoiding image distortion of the Sgr A* region due to the off-axis PSF in the mini-survey data, we only used the three observations where Sgr A*

was on-axis. Figure 5 shows the 20–40 keV *NuSTAR* image of the GC region. Diffuse emission from SNR Sgr A East (red contours in Figure 5), which is comprised of a $kT \approx 1$ keV and $kT \approx$ 3–6 keV two-temperature thermal plasma (Sakano et al. 2004; Park et al. 2005), is no longer visible.

Instead, the central ~ 10 parsec of the persistent 20–40 keV emission is dominated by a point-like feature and a previously unknown diffuse X-ray component in the hard X-ray band (Perez et al. 2015). Perez et al. (2015) fit the raw count *NuSTAR* image in the 20–40 keV band with a two-dimensional model with two Gaussian profiles. The fitting range was restricted to the central $3'$ to minimize the effect of background variations between different detector chips and bias from the molecular cloud region to the northeast. The fitting procedure used the *Sherpa* package (Freeman et al. 2001) to fully convolve the on-axis *NuSTAR* PSF, telescope pointing fluctuation and vignetting function as well as fit a flat background component together.
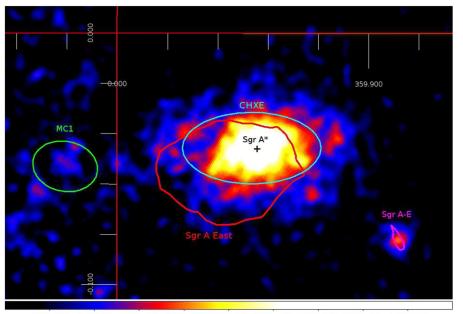
Figure 6 shows *NuSTAR* 20–40 keV image zoomed in the central $3'$ region around Sgr A*. The dominant feature is not resolved by *NuSTAR* and therefore consistent with a point source, and its centroid at R.A. = $17^h45^m39\overset{s}{.}76$ and decl. = $-29°00'20\overset{''}{.}2$ (J2000; white dashed circle in Figure 6 indicating 90% c.l position error of $7''$) aligns well with the head of the PWN candidate G359.95–0.04. The compact size of G359.95–0.04 with $\sim 6''$ elongation as measured at $E < 8$ keV band by *Chandra* (Wang et al. 2006; thus basically a point source with the $\sim 1'$ *NuSTAR* HPD) and spatial coincidence suggests that G359.95–0.04 is the likely counterpart to this point-like hard X-ray emission. This is further supported by our spectral analysis (Section 7) and the fact that the head of G359.95–0.04 has the hardest power-law spectrum and the highest 2–8 keV flux in the filament (Wang et al. 2006).

On the other hand, the central hard X-ray emission (CHXE) is centered at R.A. = $17^h45^m40\overset{s}{.}24$ and decl. = $-29°00'20\overset{''}{.}7$ (J2000; green dashed circle in Figure 6 indicating 90% c.l position error of $11''$), and it has an extent (FWHM) of $l = 3\overset{'}{.}3$ and $b = 1\overset{'}{.}7$ or 8 and 4 pc assuming a GC distance of 8 kpc (cyan ellipse in Figure 5). According to the detailed spectral study of two nearby intermediate polars and the CHXE by Hailey et al. (2015), the CHXE emission is likely an unresolved population of intermediate polars with white dwarf masses $M_{WD} \sim 0.9 M_\odot$.

4.3. 40–79 keV Band Morphology

The only significant emission above 40 keV in this field is concentrated within the central $1'$ region of the GC, likely because the three Sgr A* observations have a longer combined exposure than the *NuSTAR* mini-survey (Figure 1). Figure 7 shows a *NuSTAR* exposure-corrected smoothed image and the matching trial map of the central $1'$ region around Sgr A* in the 40–79 keV band, which is the only region with significant emission in this band. Given the fewer source counts, we smoothed the *NuSTAR* image with a larger Gaussian width of $17\overset{''}{.}5$ (7 pixels) for better illustration. The view of the GC drastically simplifies above 40 keV—the emission is centered around G359.95–0.04 with some potential substructures.

The trial map clearly exhibits two distinct features above the 4σ level. One is a point-like feature centered at the head of G359.95–0.04 and also spacially coincident with the TeV source HESS J1745–290. This feature is persistent, observed in

Figure 5. *NuSTAR* 20–40 keV exposure-corrected smoothed image of the central $10' \times 7'$ region around Sgr A* in the Galactic coordinates [°]. The image is overlaid with the CHXE (cyan; the FWHM ellipse), Sgr A* (black), MC1 (green), Sgr A-E (magenta), and SNR Sgr A East non-thermal radio shell contours from 20 cm observation (red). Outside this region, only the LMXB 1E1743.1–2843 is visible above 20 keV.
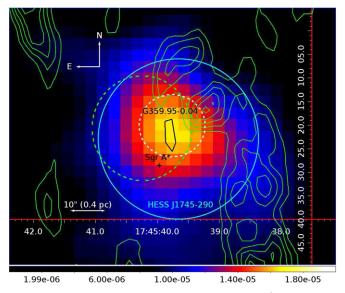

Figure 6. *NuSTAR* 20–40 keV image zoomed in the central $3'$ region overlaid with Sgr A* (black cross), the centroid of the TeV source HESS J1745–290 (cyan circle), PWN candidate G359.95–0.04 (black polygon), and circum-nuclear disk (green contours). The centroid of the CHXE and point source detected in the 20–40 keV band are indicated by green and white dashed circles with the 90% c.l. circles including both statistical and systematic errors, respectively.

all individual observations. The other is a protrusion elongated in the south–west direction. Its significance is highest in the FPMA data of one of the Sgr A* observations (ObsID: 30001002003), and thus the protrusion should be taken with some caution as a potential artifact. The protrusion is not spatially coincident with the radio (Yusef-Zadeh et al. 2012) or X-ray jets (Li et al. 2013), but it intersects with the cooler molecular gas of the circumnuclear disk indicated by green contours (Morris & Serabyn 1996; Christopher et al. 2005).

There is no apparent counterpart in either the *Chandra* 2–8 keV image or the *XMM-Newton* 6.4 keV Fe Kα image. It is possible that soft X-ray emission from the protrusion may be heavily absorbed by the optically thick circumnuclear disk and also contaminated by 8 keV thermal emission.

5. NON-THERMAL X-RAY FILAMENTS

Throughout the Sgr A* and GC mini-survey observations, *NuSTAR* detected four non-thermal X-ray filaments (G359.89–0.08 or Sgr A-E, G359.97–0.038, G0.13–0.11 and G359.95–0.04) above 10 keV. The 20–40 keV trial map (Figure 8), where Sgr A East diffuse emission is no longer dominant, illustrates the filaments Sgr A-E and G359.97–0.038. On the other hand, G0.13–0.11 is located in the molecular cloud G0.11–0.11 and it was detected by the mini-survey observation (shown as one of the green polygons in Figure 3). G359.95–0.04, which lies $9''$ away from Sgr A*, appears in the zoomed images around Sgr A* shown in Sections 4.2 and 4.3. These hard X-ray filaments are among the brightest in the soft X-ray band with 2–8 keV fluxes above 1×10^{-13} erg cm^{-2} s^{-1} or an unabsorbed luminosity of 8×10^{32} erg s^{-1} at a distance of 8 kpc (Johnson et al. 2009). Although we detected hard X-ray emission from a part of G359.964–0.052 shown in Figure 8, its spectral identification as the known X-ray filament is unclear since it might be confused with a bright *Chandra* source CXO J174543.7–285947 with $F_{\gamma,2-8\mathrm{keV}} = 6.8 \times 10^{-6}$ photons cm^{-2} s^{-1} within $\sim 10''$ of the filament (Muno et al. 2009), in addition to some contamination from 8 keV thermal emission and the CHXE. In the following sections, we individually discuss three out of the four hard X-ray filaments detected by *NuSTAR* above 10 keV. G359.95–0.04 will be later discussed in connection with the TeV source HESS J1745–290 (Section 7).
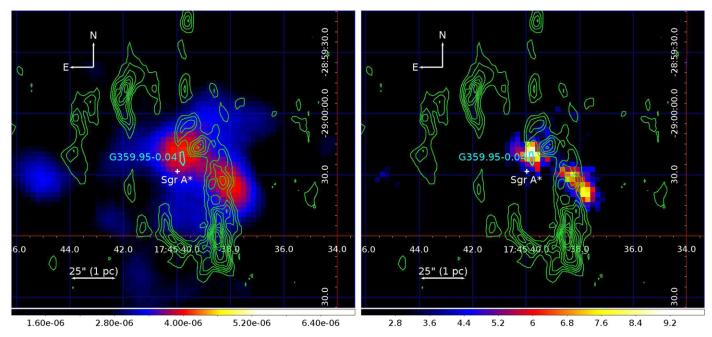
Figure 7. *NuSTAR* 40–79 keV exposure-corrected image (left) and trial probability map (right) of the central 1 arcmin region around the GC overlaid with PWN candidate G359.95–0.04 (cyan polygon), Sgr A* (white cross), and circumnuclear disk contours (green). The circumnuclear disk contours were obtained from OVRO HCN map (Christopher et al. 2005). The exposure-corrected image was smoothed by a Gaussian kernel with 7 pixel (17″.5) width, while the trial map is unsmoothed. In the trial map, 3, 4, and 5σ detections correspond to values of 6.1 (orange), 7.8 (yellow), and 9.1 (white) respectively.
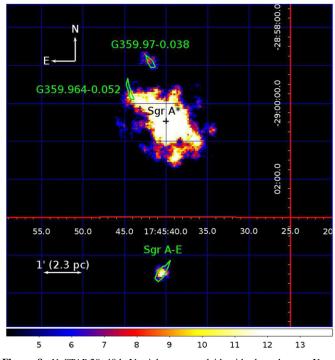

Figure 8. *NuSTAR* 20–40 keV trial map overlaid with three known X-ray filaments (green polygons). The polygons roughly traces the 2–8 keV morphologies of the filaments determined with *Chandra*. The image scale was chosen from $\log(P_{\rm trial}) = 4$ to 15 to illustrate the *NuSTAR* filaments. $\log(P_{\rm trial}) > 9.1$ (orange color bar) indicates above 5σ detection.

5.1. G359.89–0.08 (Sgr A-E)—TeV Electrons Trapped in Magnetic Tubes

G359.89–0.08 is the brightest X-ray filament, with a 3–79 keV flux of 2.0×10^{-12} erg cm^{-2} s^{-1} or an unabsorbed X-ray luminosity of 2.6×10^{34} erg s^{-1} assuming a distance of 8 kpc (Zhang et al. 2014). The filament was detected up to $\sim$50 keV with a best-fit power-law index of $\Gamma = 2.3 \pm 0.2$. We do not detect another prominent radio filament Sgr A-F (G359.90–0.06), above 10 keV. This is consistent with the fact that Sgr A-F is significantly fainter than G359.89–0.08 (Lu et al. 2008). Based on the high-resolution radio and X-ray morphology of the filament as well as spectral analysis, Zhang et al. (2014) ruled out both a PWN scenario and a SNR-molecular cloud interaction. Instead, the most plausible scenario is that magnetic flux tubes trap $\sim$100 TeV electrons, which emits synchrotron X-rays up to $\sim$50 keV. Since $\sim$100 TeV electrons have cooling times as short as $\sim$1 year for $B \sim 0.1$ mG, electrons must be accelerated nearby before entering the filament. One possible external source of TeV electrons is relativistic protons accelerated from Sgr A* or SNRs interacting with the nearby 20 km s^{-1} cloud which produces secondary electrons via pion decays. The electrons can diffuse out of the cloud before they cool significantly by synchrotron radiation, and become trapped in the magnetic flux tubes. Another (less likely) possibility is that a population of unresolved $\sim$10^5 year old PWNe accelerate electrons to TeV energies. *Suzaku* has detected extended X-ray emission from such $\sim$10^5 year-old PWNe elsewhere in the Galactic Plane (Bamba et al. 2010), but low brightness X-ray emission from old PWNe may be contaminated by the strong GC diffuse emission or be below the *NuSTAR* detection level. We therefore cannot completely rule out this scenario.

5.2. G359.97–0.038—The Sgr A East Shell interacting with the 50 km s^{-1} Cloud

G359.97–0.038 is located just outside the Sgr A East shell, and it is close to the "Plume" region. By jointly fitting the *NuSTAR* and *Chandra* spectra of the filament, Nynka et al. (2015) found that its non-thermal spectrum extends to $\sim$50 keV with the best-fit photon index $\Gamma = 1.3^{+0.3}_{-0.2}$. The photon index of

this filament is significantly harder than that of G359.89–0.08 ($\Gamma = 2.3 \pm 0.2$). Using the high-resolution radio and *Chandra* image of the filament as well as spectral energy distribution (SED) model fitting including the *NuSTAR* results, Nynka et al. (2015) found that the PWN scenario is again highly unlikely. Instead, the filament is likely illuminated by the interaction between the shell of SNR Sgr A East and the $50 \, \mathrm{km \, s^{-1}}$ cloud (Nynka et al. 2015), as evidenced by the large width of the CS $J = 1$–0 line, which exceeds the cloud bulk velocity of $\sim 50 \, \mathrm{km \, s^{-1}}$ (Tsuboi et al. 2006). The harder X-ray power-law spectrum of $\Gamma = 1.3$ is typical of non-thermal bremsstrahlung or inverse Compton emission of electrons accelerated at the SNR–cloud interaction site (Bykov et al. 2000, 2005). The lack of an apparent radio counterpart is also consistent with this picture. The GeV source 2FGL J1745.6–2858 detected by *Fermi* is coincident with the position of G359.97–0.038 (Nolan et al. 2012; Yusef-Zadeh et al. 2013). If the GeV source is associated with G359.97–0.038, it is additional evidence supporting the SNR–cloud interaction scenario since the SED model of Bykov et al. (2000) predicts a peak in the GeV band.

5.3. G0.13–0.11—PWN?

The third hard X-ray filament G0.13–0.11, shown in Figure 3, is located near the Radio Arc region and is embedded in the molecular cloud G0.11–0.11. The filament is a candidate PWN due to its cometary shape and a point-like feature CXOGCS J174621.5–285256 (Wang et al. 2002b). It is one of the few X-ray filaments that has a radio counterpart. It is not possible to extract a clean *NuSTAR* spectrum of the filament due to the limited statistics, and contamination from the bright X-ray source CXOUGC J174622.7–285218, $\sim 40''$ away from the filament. CXOUGC J174622.7–285218 is a magnetic CV with a 1745 s periodicity (Muno et al. 2009) and *NuSTAR* detected its hard X-ray extension above 10 keV (Hong et al. 2015). A deeper *NuSTAR* observation with more than ~ 200 ks exposure will be required to perform useful spectral and timing analyses of this filament.

5.4. Heterogeneous Origin of Non-thermal X-Ray Filaments?

Two of the three hard X-ray filaments (G359.89–0.08 and G359.97–0.038) detected above 10 keV are unlikely to be PWNe, suggesting a heterogeneous origin for the X-ray filaments. G359.89–0.08 is likely powered by synchrotron radiation in magnetic flux tubes trapping TeV electrons, while G359.97–0.038 is illuminated by Sgr A East interacting with a $50 \, \mathrm{km \, s^{-1}}$ cloud. Our results indicate a reservoir of relativistic electrons and protons in the central 10 pc region, rather than production and acceleration of particles locally inside the filaments as in the PWN scenario. Electrons may be accelerated to TeV energies by faint $\sim 10^5$ year-old PWNe or they are by-products of hadronic interactions between relativistic protons and clouds.

Alternatively, Linden et al. (2011) proposed dark matter annihilation as a potential source of GeV electrons that are trapped in magnetic flux tubes and emit synchrotron radiation. In this scenario, light neutralinos with ~ 5–10 GeV mass annihilate directly to leptons that decay to GeV electrons. The four radio filaments (G0.2–0.0, G0.16–0.14, G0.08+0.15 and G359.1–0.2) investigated by Linden et al. (2011) using their model are located outside the *NuSTAR* GC survey area or did not have sufficiently long exposure time in the *NuSTAR* mini-survey coverage to warrant study. Deep X-ray observations of these radio filaments could test the dark matter scenario since any X-ray detection of these radio filaments would indicate the presence of TeV electrons that cannot be produced in the annihilation of ~ 5–10 GeV mass neutralinos. A more extensive hard X-ray survey of radio and X-ray filaments probe not only the spatial and energy distribution of cosmic-rays beyond the central 10 pc region but also dark matter physics.

6. GALACTIC CENTER MOLECULAR CLOUDS

All Sgr A clouds, including MC1, MC2, the Bridge and G0.11–0.11, were covered by the *NuSTAR* mini-survey as well as *XMM-Newton* observations in 2012. As Figure 3 in Section 4.1 shows, we find that Fe Kα line emission (as measured by *XMM-Newton*) and hard X-ray continuum (as measured by *NuSTAR*) emission are spatially well-correlated in MC1, the Bridge and the Arches cluster. In 2013 October, a 300 ks *NuSTAR* observation of the fading Sgr B2 spatially resolved hard X-ray emission from the Sgr B2 core and a newly discovered cloud feature G0.66–0.13 (Zhang et al. 2015). Sgr C is not suitable for *NuSTAR* observations because of strong ghost-ray background from the bright persistent LMXB 1A1742–294.

Two models, the so-called XRN model (Sunyaev et al. 1993) and the LECR model (Yusef-Zadeh et al. 2002a), predict distinct spectral and temporal properties for the X-ray emission from GCMCs. In the XRN scenario, molecular clouds can reflect X-rays from an illuminating source by scattering continuum X-rays and producing fluorescence line emission following photo-ionization of K-shell electrons. The XRN model predicts (1) variability of Fe Kα line and X-ray continuum emission over the light-crossing time of a cloud (~ 1–10 years) or over the variability timescale of an illuminating source, (2) a strong Fe Kα line with equivalent width (EW) $\gtrsim 1$ keV, (3) a Fe–K photo-absorption edge at 7.1 keV and (4) a Compton reflection hump (i.e., curved power-law spectrum) in the hard X-ray band if the cloud column density is high ($N_\mathrm{H} \gg 10^{24} \, \mathrm{cm^{-2}}$). Alternatively, low-energy cosmic ray electrons (LECRe), protons and ions (LECRp) can eject K-shell electrons via collisional ionization leading to fluorescence line emission. The LECR model predicts (1) a power-law spectrum originating from non-thermal bremsstrahlung emission, (2) an Fe Kα line with EW $\lesssim (0.25$–0.4$) \, Z_\mathrm{Fe}$ keV where Z_Fe is the Fe abundance relative to solar (Yusef-Zadeh et al. 2007, 2013), and (3) time variability of Fe Kα line and X-ray continuum emission over the electron cooling/diffusion time (LECRe) or long-term variability over $\gtrsim 100$ years (LECRp). The shape of the X-ray continuum is sensitive to the incident cosmic ray energy spectrum.

Previous soft X-ray observations have been mainly focused on tracking time evolution of Fe K-α line at 6.4 keV (see Ponti et al. 2013, for a review), due to their narrow bandpass (typically ~ 4–8 keV) where different spectral components such as diffuse thermal emission, X-ray continuum from the cloud, Fe K edge and Fe K fluorescent lines are potentially all present and strongly degenerate. Both the EW of the Fe Kα line and the absorption depth (τ_FeK) of the Fe K edge are highly sensitive to the underlying X-ray continuum level. Diffuse thermal emission, if not properly subtracted, will enhance the underlying continuum level and thus decrease both the Fe Kα line EW and τ_FeK. However, in the previous *XMM-Newton*,

Chandra and *Suzaku* analysis, intrinsic X-ray continuum spectra either have been poorly constrained (Inui et al. 2009; Ponti et al. 2010; Nobukawa et al. 2011) or have been assumed to be a power-law spectrum with Γ fixed to 1.9 (Capelli et al. 2012). More importantly, previous X-ray studies determined the parameters of the GCMCs and illuminating X-ray sources separately from individual components such as the Fe Kα line or absorption edge, therefore they lack self-consistency. In the XRN scenario, an Fe Kα line flux measurement yields a luminosity of the illuminating primary souce only at ∼8 keV with some uncertainty associated with Fe abundance (Sunyaev et al. 1993).

In contrast, a broadband X-ray continuum measurement provides the most robust determination of the X-ray spectrum of the primary source in the XRN scenario and a cosmic ray energy spectrum in the LECR scenario. The hard X-ray continuum provides an excellent measurement of the intrinsic column density ($N_{\rm H}$) of the cloud (Ponti et al. 2014). In the subsequent sections, we fit self-consistent spectral models to the broadband X-ray spectra of the Sgr A clouds using the *NuSTAR* and *XMM-Newton* data. This provides a powerful diagnostic that can distinguish between different models and tightly constrain parameters since it takes the full advantage of the broadband X-ray spectroscopy.

6.1. Spectral Analysis of the Sgr A Clouds: MC1 and the Bridge

We extracted *NuSTAR* and *XMM-Newton* EPIC-PN source spectra of MC1 and the Bridge using the same regions quoted in Ponti et al. (2010), as indicated by the green regions in Figure 3. *XMM-Newton* observations 0694641101 (35.5 ks total exposure) and 0694640401 (43.9 ks total exposure) were used for MC1 and the Bridge respectively since the sources are not intercepted by detector gaps and the signal-to-noise ratio is highest in these observations. This allows us to extend our energy band to 10 keV for the *XMM-Newton* spectra, while the background dominates above ∼8 keV in the other observations. We selected appropriate *NuSTAR* observations and focal plane module data that cover the full extent of the clouds that are free from high background counts. We extracted MC1 source spectra from FPMA data of one Sgr A* observation (ObsID: 30001002004) and three mini-survey observations (ObsID: 40010001002, 40010002001, and 40010004001), for a total exposure time of 125.7 ks. We extracted the Bridge spectra from FPMA data of three *NuSTAR* mini-survey observation (ObsID: 0010003001, 0010004001 and 40010006001) with a total exposure time of 71.5 ks. Although there are two bright regions in the Bridge (the so-called Br1 and Br2 region in Capelli et al. 2012), separate spectral analysis of each region does not yield sufficient photon statistics. Since we are not certain whether SLB or focused diffuse emission dominates as the background of these regions, we applied both the conventional and off-source background subtraction methods described in the Appendix. We found that the final results were not significantly different between the two methods because the contribution of SLB and focused diffuse emission is similar in these molecular cloud regions.

We fit the joint *XMM-Newton* and *NuSTAR* spectra with XSPEC models based on the XRN and LECR scenarios. For all spectral models considered here, we applied tbabs*[apec + apec + cloud_model] where cloud_model represents one of the X-ray spectral models

that are intrinsic to the GCMCs and described in the subsequent sections. In either case, the common model components are tbabs and two apec models representing foreground (galactic) absorption, $kT \sim 1$ and $kT \sim 8$ keV thermal components in the GC, respectively. We linked all the fit parameters between the *XMM-Newton* and *NuSTAR* spectra except the flux normalizations for the two thermal (apec) model components since background spectra mostly composed of the two thermal components were extracted differently for the *XMM-Newton* and *NuSTAR* spectra. Hereafter, we present the best-fit flux normalizations of the two thermal components from the *XMM-Newton* spectral fitting.

For the LECR scenario, we fit a self-consistent X-ray spectral model available in XSPEC for both the LECR electron and proton cases, by taking into account both X-ray continuum and fluorescent line components calculated from the energy loss of cosmic-rays penerating into a slab-like cloud of neutral gas at a constant rate (Tatischeff et al. 2012). Since the observed year-scale time variability of Fe Kα line flux in the Sgr A clouds rules out the LECR proton scenario, we fit an absorbed LECR electron model (tbabs*lecre) as the intrinsic cloud model cloud_model.[24] Following Tatischeff et al. (2012) and Krivonos et al. (2014), we fixed the path length of cosmic-ray electrons to $\Lambda = 5 \times 10^{24}$ cm^{-2} since we find that the fitting results are insensitive to Λ. In all cases, the LECRe models do not fit the *XMM-Newton* and *NuSTAR* spectra for MC1 and the Bridge as well as the XRN models, yielding $\chi^2_\nu = 1.2$–1.4 (Figures 9 and 10). The spectral fitting requires unreasonably high metallicity $Z \approx 4$ in order for the LECRe model to account for the strong Fe Kα line. Therefore, we conclude that the LECRe models are not consistent with the X-ray spectra of the two Sgr A clouds.

6.2. Spectral fitting Results with MYTorus Model

Hereafter we present spectral fitting results primarily with MYTorus model, which is the only Monte-Carlo based XRN model that is available in XSPEC with finite cloud column density (Murphy & Yaqoob 2009; Yaqoob 2012). Unlike other XRN models that have been applied to GCMC X-ray data, the MYTorus model can determine the cloud and primary X-ray source parameters self-consistently. Indeed, we find that the MYTorus model yields better spectral fits than the other XRN models as shown in this section. The Appendix fully describes the MYTorus model application to the GCMC X-ray data and compare it with other widely used XRN models. For comparison between the different models and also with the previous results, we present the fit results using an ad hoc XRN model tbabs*(powerlaw + gauss + gauss) and a slab geometry model reflionx with infinite optical depth (Magdziarz & Zdziarski 1995; Ross & Fabian 2005; Nandra et al. 2007). Other slab geometry models such as pexmon yield similar results. In the ad hoc XRN model, we fixed the line

---

[24] A similar model was used to fit X-ray spectra of Sgr B2 clouds (Terrier et al. 2010; Zhang et al. 2015). The photo-absorption term takes into acount intrinsic absorption in the cloud with a characteristic column density $N_{\rm H}$. Although Fe K-shell electrons are ionized by cosmic-rays coming from an external source, continuum X-rays emitted via non-thermal bremsstrahlung can undergo photo-absorption before escaping from the cloud. We also set $N_{\rm H} = 0$ for the opposite case where continuum X-rays are emitted near the surface of the cloud, in which case most of them are not absorbed in the cloud. Although this is not a self-consistent treatment of the intrinsic absorption in the cloud, the two cases should bound the problem where the radiative transfer of continuum X-ray photons is not considered in the LECR models.
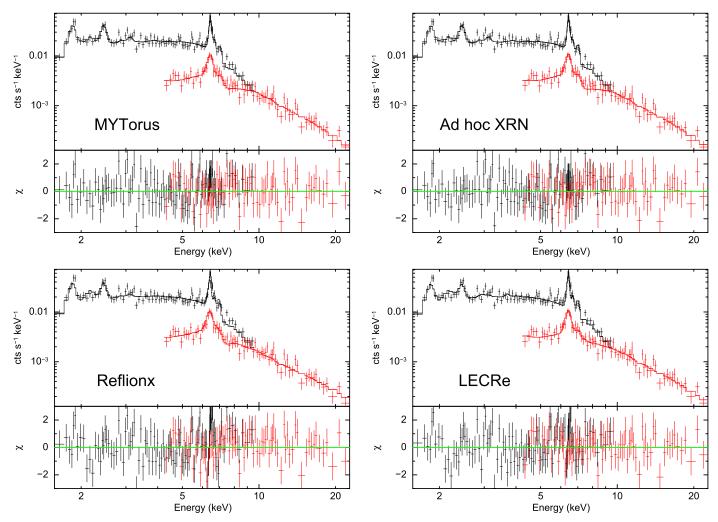
Figure 9. 1.5–20 keV *XMM-Newton* (black) and *NuSTAR* (red) spectra of MC1 fit with the MYTorus (upper left), ad hoc XRN (upper right), reflionx (lower left), and LECR electron model (lower right).

energy and width of (weak) Fe Kβ line to 7.06 and 0.01 keV, respectively and linked its flux normalization to that of Fe Kα line multiplied by 0.15, i.e., the ratio of the Kα and Kβ line fluorescence yields (Murakami et al. 2001).

The MYTorus model includes three components, namely the transmitted continuum (MYTZ), scattered continuum (MYTS) and Fe fluorescent emission lines (MYTL), in a range of equatorial hydrogen column density through the tube of the torus $N_{\rm H} = 10^{22}$–10^{25} cm^{-2}, power-law photon index $\Gamma = 1.4$–2.6 and incident angle (between an observer and the symmetry axis of the torus) $\theta_{\rm obs} = 0°$–$90°$. See Figure 15 in the Appendix for the geometry of the MYTorus model in comparison with the conventional geometry used in many publications on GCMCs. Note that $\theta_{\rm obs} = 0°$ and $90°$ correspond to a face-on and edge-on observing view, respectively. Since we observe only the reflected X-ray emission from GC molecular clouds, we adopted two additive XSPEC models for scattered continuum (MYTS) and Fe fluorescent lines (MYTL):

```
atable{mytorus_scatteredH500_v00.fits} +
atable{mytl_V000010pEp040H500_v00.fits}
```

in a "coupled" mode where the same primary X-ray spectrum is input for the both components. We selected the MYTS and

MYTL tables with a power-law model with the highest energy cut-off at $E = 500$ keV. Following the MYTorus manual[25], we selected the MYTL data table with an energy offset of +40 [eV] since the best-fit Fe Kα line centroids with a Gaussian line profile are 6.44 [keV] probably due to slightly ionized Fe in the clouds and/or instrumental energy offset (note that *NuSTAR* has a systematic uncertainty of 40 eV near Fe emission lines Madsen et al. 2015). We bound the incident angle to $\theta_{\rm obs} \leqslant 60°$ since we find that the MYTorus model is valid to fit the X-ray spectra of GCMCs in this range (Appendix).

The MYTorus model fits the joint *XMM-Newton* and *NuSTAR* spectra of MC1 and the Bridge well, yielding $\chi^2_\nu/\mathrm{dof} = 1.01/170$ (MC1) and $1.13/524$ (the Bridge), with all parameters well constrained (Figures 9, 10 and Table 2). We found that the intrinsic absorption and power-law continuum were accurately measured only by the joint fitting of *XMM-Newton* and *NuSTAR* spectra, as a result of combining high-resolution Fe line spectroscopy from *XMM-Newton* with broadband X-ray spectroscopy from *NuSTAR*. The two thermal components have $kT_1 \sim 1$ and $kT_2 \sim 8$ keV and are consistent
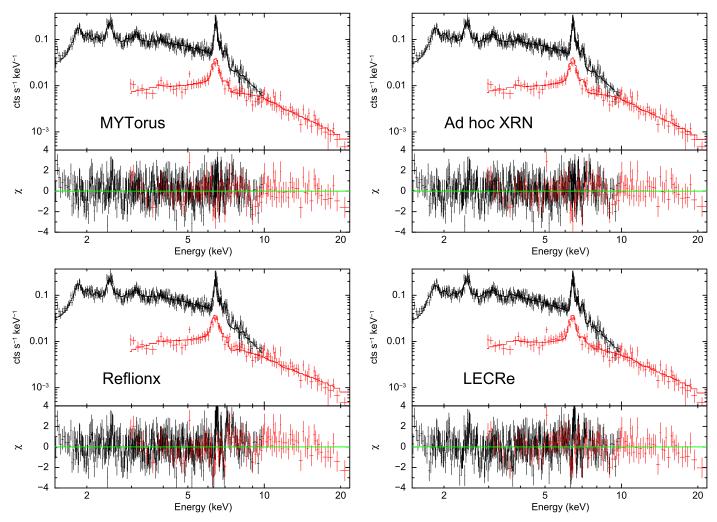

Figure 10. 1.5–20 keV *XMM-Newton* (black) and *NuSTAR* (red) spectra of the Bridge fit with the MYTorus (upper left), ad hoc XRN (upper right), reflionx (lower left), and LECR electron model (lower right).

with the previous measurements in this region (Muno et al. 2004; Koyama et al. 2007). Although the abundance for the lower $kT_1 \sim 1\,\mathrm{keV}$ temperature component is poorly constrained, we find that it does not affect the XRN model parameters. Although the ad hoc XRN model yields similar fit quality with $\chi^2_\nu/\mathrm{dof} = 1.01/168$ (MC1) and $1.16/522$ (the Bridge), the MYTorus model has fewer fit parameters due to its self-consistency—the power-law index and flux normalization are linked between the scattered continuum (MYTS) and the fluorescent line component (MYTL). The `reflionx` models do not fit MC1 and the Bridge spectra well with $\chi^2_\nu/\mathrm{dof} = 1.40/170$ and $1.60/525$, respectively. When we fit the MC1 spectra with the `reflionx` model, we fixed the plasma temperature of the second thermal component to 8 keV. Otherwise, the spectral fitting yields unreasonable parameters such as $kT_2 \sim 20\,\mathrm{keV}$ and Fe abundance higher than 10 for the `reflionx` model.

Intrinsic column density. Our joint *XMM-Newton* and *NuSTAR* analysis using the MYTorus model measured the equatorial hydrogen column density with $N_\mathrm{H} = 2.3^{+1.0}_{-0.6} \times 10^{23}$ (MC1) and $1.5^{+0.5}_{-0.3} \times 10^{23}\,\mathrm{cm}^{-2}$ (the Bridge). The ad hoc XRN model yields similar N_H values in good agreement with the results of Capelli et al. (2012), who applied a similar ad hoc XRN model. Although one cannot simply compare the N_H

values from the MYTorus model and ad hoc XRN model (which has no geometry defined for N_H), our simulation shows that spectral fitting with the ad hoc XRN model "measures" an N_H that deviates from the geometrical N_H of the MYTorus model by a factor of $\sim$2, at $N_\mathrm{H} \sim 10^{23}\,\mathrm{cm}^{-2}$ (Appendix). In comparison with the measurements of Ponti et al. (2010) (MC1: $N_\mathrm{H} \sim 4 \times 10^{22}$ and the Bridge: $9 \times 10^{22}\,\mathrm{cm}^{-2}$) based on the CS line intensity map (Tsuboi et al. 1999; Ponti et al. 2010), our N_H value for MC1 is higher by a factor of $\sim$5 while our result for the Bridge is close to their value. However, Ponti et al. (2010) and Capelli et al. (2012) pointed out the difficulty with constraining N_H using molecular emission lines. For example, CS (Amo-Baladrón et al. 2009) and H^{13}CO$^+$ (Handa et al. 2006) emission line measurements deduced nearly two orders of magnitude different N_H values for another Sgr A cloud, G0.11–0.11. Still, the measured N_H yields the Thomson depth of $\tau_T \sim 0.1$, indicating that these clouds are optically thin. Therefore, it is more accurate to apply XRN models properly suited for optically thin cases rather than the slab geometry models which assume infinite column density.

Power-law index. The power-law photon indices (with 68% c.l. errors) of the primary X-ray source are well constrained at $\Gamma = 2.11^{+0.23}_{-0.14}$ (MC1) and 1.81 ± 0.10 (the Bridge) by the MYTorus model. The systematic errors associated with the

Table 2
NuSTAR + XMM-Newton Spectral fitting Results of MC1 and the Bridge using the three XRN Models

Parameters	MC1			Bridge		
	Ad hoc XRN	reflionx	MYTorus	Ad hoc XRN	reflionx	MYTorus
N_H^f (10^{22} cm^{-2})	$7.1^{+0.7}_{-0.6}$	$8.3^{+0.5}_{-0.6}$	7.1 ± 0.7	6.1 ± 0.2	5.9 ± 0.2	6.1 ± 0.2
kT_1 (keV)	$0.62^{+0.09}_{-0.07}$	0.43 ± 0.04	$0.59^{+0.1}_{-0.04}$	0.90 ± 0.03	0.91 ± 0.02	0.91 ± 0.03
Abundance Z_1	$3.0^{+2.0}_{-1.7}$	$5.0_{-2.9}$	$5.0_{-3.3}$	$2.9^{+2.1}_{-0.9}$	$5.0_{-0.7}$	$2.8^{+1.8}_{-0.3}$
$norm_1$	$5.5^{+10.4}_{-2.8} \times 10^{-3}$	$1.4^{+2.1}_{-0.6} \times 10^{-2}$	$3.7^{+1.0}_{-0.2} \times 10^{-3}$	$8.8^{+4.2}_{-3.8} \times 10^{-3}$	$4.2^{+0.8}_{-0.4} \times 10^{-3}$	$8.9^{+3.9}_{-3.4} \times 10^{-3}$
kT_2 (keV)	$8.1^{+1.0}_{-0.5}$	8 (fixed)	$9.1^{+1.6}_{-1.5}$	$6.5^{+0.8}_{-0.6}$	$10.6^{+0.8}_{-0.6}$	$7.5^{+0.3}_{-0.7}$
Abundance Z_2	0.6 ± 0.2	$0.7^{+0.2}_{-0.1}$	0.7 ± 0.2	0.5 ± 0.1	$0.77^{+0.08}_{-0.07}$	$0.75^{+0.15}_{-0.07}$
$norm_2$	$(9.3 \pm 0.4) \times 10^{-4}$	$(1.1 \pm 0.2) \times 10^{-3}$	$9.3^{+0.2}_{-0.1} \times 10^{-4}$	$(3.4 \pm 0.4) \times 10^{-3}$	$(3.8 \pm 0.2) \times 10^{-3}$	$(2.7 \pm 0.3) \times 10^{-3}$
N_H (10^{23} cm^{-2})	2.1 ± 0.6	...	$2.3^{+1.0}_{-0.6}$	1.5 ± 4	...	$1.5^{+0.6}_{-0.3}$
PL photon index (Γ)	2.20 ± 0.15	$2.95^{+0.14}_{-0.16}$	$2.11^{+0.23}_{-0.14}$	1.81 ± 0.11	$2.29^{+1.6}_{-1.7}$	1.81 ± 0.10
PL norm[a]	$(1.5 \pm 0.5) \times 10^{-3}$	$7.3^{+5.8}_{-3.3} \times 10^{-5}$	$1.8^{+0.6}_{-0.4} \times 10^{-2}$	9.4×10^{-4}	$2.2^{+1.2}_{-0.9} \times 10^{-5}$	$(3.8 \pm 0.5) \times 10^{-2}$
Fe Kα energy (keV)	6.444 ± 0.008	...	...	6.439 ± 0.003	...	...
Fe Kα flux[b]	1.6 ± 0.1	...	...	5.6 ± 0.2	...	...
Fe Kα EW (keV)	0.93 ± 0.12	...	...	1.38 ± 0.14	...	...
Fe abundance	...	1.4 ± 0.2	1 (fixed)	...	3.8 ± 0.6	1 (fixed)
Inclination angle (°)	...	...	60_{-23}[c]	...	...	$4.5^{+15.3}_{-4.5}$
χ^2_ν (dof)	1.01 (168)	1.40 (170)	1.01 (168)	1.16 (522)	1.60 (525)	1.13 (524)

Notes. The errors are 68% confidence level. Fe Kβ line parameters are not listed since they are either fixed or linked to Fe Kα parameters. N_H^f and N_H refer to the best-fit hydrogen column density for the foreground and intrinsic absorption term in the X-ray reflection models defined in Section 6.2.
[a] Flux normalization [photons cm^{-2} s^{-1} keV^{-1}] at 1 keV. The flux normalizations are defined differently in the three XRN models. For example, the ad hoc XRN model refers to the observed X-ray flux, while the MYTorus model refers to the incident X-ray source flux. Therefore, their best-fit values cannot be simply compared with each other.
[b] Flux unit is 10^{-5} ph cm^{-2} s^{-1}.
[c] We set the upper bound of θ_{obs} to 60° since it is the valid range for the MYTorus model to approximate the spectrum of a quasi-spherical molecular cloud (Appendix).

angular dependence of the MYTorus model are smaller than the statistical errors for a measurement of Γ at $N_H = 10^{23}$ cm^{-2} (Appendix). Therefore, our results indicate that MC1 and the Bridge have consistent photon indices of the primary X-ray source at ~2σ level. The measured photon indices are both softer than those of Ponti et al. (2010): $\Gamma = 0.8^{+0.4}_{-0.5}$ for MC1 and $\Gamma = 1.0^{+1.0}_{-0.3}$ for the Bridge, based on *XMM-Newton*-only spectral analysis over a narrower band between 4 and 8 keV. The ad hoc XRN model measures similar photon indices to the MYTorus model since the clouds are optically thin and the primary X-ray spectrum shape is not significantly perturbed by photo-absorption and Compton scattering. The reflionx model yields softer photon indices ($\Gamma = 3.0$ and 2.3 for MC1 and the Bridge, respectively). Due to the infinite column density assumed in the reflionx model, low energy photons are overly absorbed thus requiring a softer power-law photon index to fit the X-ray spectra as similarly observed in *NuSTAR* spectral analysis of the Arches cluster and Sgr B2 (Krivonos et al. 2014; Zhang et al. 2015).

Fe Kα fluorescent line. Both the flux and the EW of the Fe Kα fluorescent line have often been used to track the time evolution of GC molecular clouds. Among our spectral models, only the ad hoc XRN model can provide Fe Kα line parameters separately since the Fe fluorescent lines and scattered continuum are coupled in the self-consistent models, which are not parameterized to easily provide Fe K fluorescent line fluxes or EWs in XSPEC. Using the fit results with the ad hoc XRN model, we calculated the Fe Kα line EW with respect to the power-law continuum, which is the only component instrinsic to the clouds and thus can be compared to the predictions from the XRN and LECR models (Section 6). For comparison with other results, it is crucial to specify which X-ray continuum component is used to calculate the Fe Kα line EW. Our EW values, 0.93 ± 0.12 (MC1) and 1.38 ± 0.14 keV (the Bridge), are larger than those of Ponti et al. (2010): 0.68 (MC1) and 0.75 keV (the Bridge), while the best-fit Kα line flux normalizations are consistent between our work and Ponti et al. (2010). Note that the Fe Kα line flux from the entire MC1 cloud has stayed nearly constant for years, although *Chandra* found different time variations across the cloud (Clavel et al. 2013). The discrepancy in Fe Kα line EWs is likely due to the fact that *XMM-Newton* continuum spectra are heavily contaminated by diffuse thermal emission, thus the continuum level is enhanced compared to the intrinsic non-thermal emission from the cloud. Indeed, using the Fe Kα line flux normalization and the power-law continuum parameters from Table 3 in Ponti et al. (2010), we obtain EW = 0.83 keV (MC1) and 1.16 keV (the Bridge)—they are similar to our measurements. Our Fe Kα line EW for MC1 is also consistent with Capelli et al. (2012), who measured EW = 0.9 ± 0.1 keV.

Inclination angle. The inclination angle is constrained to $\theta_{obs} = 4°.5^{+15}_{-4.5}$ for the Bridge, while $\theta_{obs} = 60°_{-23}$ is less constrained for MC1 likely because the overall X-ray reflection spectrum is rather insensitive to θ_{obs} at $N_H \lesssim 10^{24}$ cm^{-2} (Appendix) and the MC1 data have poorer photon statistics than the Bridge data. While it is tempting to suggest the Bridge with the best-fit $\theta_{obs} \approx 0°$ is located close to the projection plane of the primary source, we cannot uniquely infer line of sight (LOS) location of the cloud based on the measured inclination angle and also we cannot estimate systematic errors on θ_{obs} in the MYTorus model (Appendix). A precise measurement of the cloud LOS location should be performed with an improved XRN model implementing more realistic geometry for the Sgr A clouds in the future.

Table 3
Comparison of Molecular Cloud and Primary source Parameters between MC1, the Bridge and Sgr B2 core using self-consistent XRN Models

Parameters	MC1	Bridge	Sgr B2
Cloud angular size S (arcmin^2)	2.1	8.5	64
Projected distance from Sgr A* (pc)	$\sim$12	$\sim$20	$\sim$100
Equatorial column density N_H (10^{23} cm^{-2})	$2.3^{+1.0}_{-0.6}$	$1.5^{+0.6}_{-0.3}$	6.8 ± 0.5
PL photon index (Γ)	$2.11^{+0.23}_{-0.14}$	1.81 ± 0.10	2.0 ± 0.2
L_X (erg s^{-1}) (2–20 keV)	$\geqslant 1.1 \times 10^{38}$ [a]	$\geqslant 0.9 \times 10^{38}$ [a]	$1.0^{+0.8}_{-0.5} \times 10^{39}$ [b]

Notes. The errors are 68% confidence level for MC1 and the Bridge, while the error confidence level for the Sgr B2 results was not specified in Terrier et al. (2010).
[a] The lower bound of L_X was determined from the best-fit parameters at $\theta_{obs} = 0°$ where the cloud is located in the same projection plane of Sgr A*.
[b] The errors are associated with the line of sight distance measurement of 130 ± 60 pc by Reid et al. (2009). The X-ray luminosity quoted in the 1–100 keV band (Terrier et al. 2010) was converted to the 2–20 keV band to match with our results for the Sgr A clouds.

6.3. Implications for the Primary Source illuminating the Sgr A Clouds

Table 3 summarizes the observed and derived parameters from MC1 and the Bridge using the self-consistent MYTorus model as well as the known geometrical parameters. For comparison with the Sgr A clouds, we adopted the Sgr B2 results from the 2003–2004 *XMM-Newton* and *INTEGRAL* observations (Terrier et al. 2010) soon after both the hard X-ray continuum and Fe Kα line fluxes started decaying in 2000, therefore they can determine the primary X-ray source spectra more accurately than the *NuSTAR* observation in 2012. Terrier et al. (2010) fit 2–100 keV spectra of a $r = 4\rlap{.}'5$ circular region centered at the core of the cloud using a self-consistent XRN model, yielding the power-law index $\Gamma = 2.0 \pm 0.2$ and 1–100 keV luminosity $L_X = 1.1 \times 10^{39}$ erg^{-1} of an illuminating X-ray source (Table 3).[26] Similar results ($\Gamma = 1.8 \pm 0.2$ and $L_X \sim 10^{39}$ erg s^{-1}) were obtained by Revnivtsev et al. (2004) who analyzed *ASCA*, *GRANAT* and *INTEGRAL* data from a larger region ($r = 6\rlap{.}'5$) in Sgr B2 using a self-consistent XRN model.

MC1, the Bridge and Sgr B2 cloud have the consistent primary power-law indice $\Gamma \sim 2$. Since θ_{obs} cannot be uniquely associated with the light-of-sight location of a cloud, the MYTorus model can give a lower bound of the illuminating source luminosity L_X in which case the cloud and the primary X-ray source are located in the same projection plane. Using the best-fit primary X-ray fluxes at $\theta_{obs} = 0°$, we determined $L_X \geqslant 1.1 \times 10^{38}$ (MC1) and 0.9×10^{38} erg s^{-1} (the Bridge). Here, we assumed that the illuminating X-ray source is located at Sgr A* and we rescaled the primary X-ray flux following the recipe in the Appendix. For reference, using the observed Fe Kα line flux (which is also subject to Fe abundance uncertainty), Clavel et al. (2013) inferred higher X-ray luminosity of 5×10^{38} erg s^{-1} for MC1 since their estimate was based on the lower cloud column density ($N_H = 4 \times 10^{22}$ cm^{-2}) determined from the CS molecular line measurements (Ponti et al. 2010) contrary to our direct measurements of N_H by fitting the broadband X-ray spectra.

Given that MC1 and the Bridge require L_X as low as $\sim 10^{38}$ erg s^{-1}, it is possible that an outbursting X-ray transient could have illuminated these clouds. Previously, *Chandra*

found short temporal evolution of two Fe Kα features in G0.11–0.11, and their Fe Kα emission was attributed to reflection of an outburst of Sgr A* or an X-ray binary with a few year duration (Muno et al. 2007). Also, Capelli et al. (2012) proposed that one of the Sgr A clouds emitting an Fe Kα line could be illuminated by the nearby X-ray transient XMMU J174554.4–285456. Within the inner 10′ of the GC, about a dozen X-ray transients have been detected, with their maximum 2–10 keV luminosities ranging from $\sim 1 \times 10^{34}$ to $\sim 7 \times 10^{38}$ erg s^{-1} (Muno et al. 2005; Degenaar et al. 2012). Only 1A 1742–289 had its maximum outburst X-ray luminosity (7×10^{38} erg s^{-1}) exceed the inferred L_X for MC1 and the Bridge. The only outburst from 1A 1742–289, observed in 1975, decayed rapidly over a few months (Branduardi et al. 1976), which is far shorter than the time variation of Fe Kα line flux observed from MC1 and the Bridge (Clavel et al. 2013). Similarly, none of the other X-ray transients in the GC had persistent outbursts over a long enough period ($\gtrsim 10$ years) to illuminate MC1 and the Bridge at the observed flux levels. In general, it is extremely rare for a bright outburst with $L_X \gtrsim 10^{36}$ erg s^{-1} to last for a few years (Chen et al. 1997). Therefore, we rule out the known X-ray transients in the GC as primary sources for MC1 and the Bridge. Alternatively, an undetected X-ray transient with X-ray outburst luminosity $L_X \gtrsim 10^{37}$ erg s^{-1} and ~ 10 year burst duration, such as the black hole binary GRS 1915+105 (Fender & Belloni 2004), could be a primary source. However, Clavel et al. (2013) found this scenario implausible since it requires unrealistic cloud distribution around the GC to account for the observed Fe Kα flux variation in the Sgr A clouds.

As a result, Sgr A* is the most likely illuminating source for MC1 and the Bridge. This is supported by the fact that the measured power-law indices ($\Gamma = 1.8$–2.1) for Sgr A clouds as well as $\Gamma = 2.0$ for Sgr B2 (Terrier et al. 2010) are consistent with those from the current Sgr A* flares (Baganoff et al. 2001; Nowak et al. 2012; Degenaar et al. 2013; Neilsen et al. 2013; Barrière et al. 2014), and low-luminosity active galactic nuclei (AGNs) typically with $\Gamma \sim 1.9$ (Reeves & Turner 2000). Several studies based on Fe Kα line and X-ray continuum flux measurements suggest that Sgr B2 was illuminated by a giant Sgr A* flare with $L_X \sim 10^{39}$ erg s^{-1} about 100 years ago (Koyama et al. 1996; Murakami et al. 2001; Ponti et al. 2010; Terrier et al. 2010; Capelli et al. 2012). Based on the different temporal variations of Fe Kα line emission from various GCMCs, Capelli et al. (2012) and Clavel et al. (2013) claimed that Sgr A* flaring activity in the past hundred years had multiple distinct periods with vastly different flaring powers before declining to the current flaring state with

---

[26] The projected distance of 100 pc between Sgr A* and Sgr B2 was assumed for L_X. The intrinsic column density $N_H = 6.8 \pm 0.5$ cm^{-2} was also measured using an adhoc XRN model `wabs*(apec+gaus+gaus+wabs*pegpw)` (Terrier et al. 2010). Since the hydrogen column density distribution is highly non-uniform in the Sgr B2 region (Etxaluze et al. 2013), N_H measured by X-ray spectral fitting may vary in the range of $\sim 10^{23}$–10^{25} cm^{-2} depending on a choice of the extraction region (Zhang et al. 2015).

$L_X \lesssim 5 \times 10^{35}$ erg s^{-1} (Nowak et al. 2012). Given the error bars in Γ and the lower bounds of L_X in Table 3, our analysis shows that the primary X-ray spectra are consistent between MC1, the Bridge and Sgr B2, thus it is still inconclusive whether these clouds were illuminated by different Sgr A* flares in the past or not. Continuing long-term monitoring of the Sgr A clouds by *NuSTAR*, with improved XRN models and photon statistics, will be able to constrain Sgr A* flaring activity (e.g., number of giant Sgr A* flares, their X-ray luminosities, and durations) over the last few hundred years more tightly.

7. THE CENTRAL 10 pc AROUND SGR A*

The central 10 pc around Sgr A* is a highly crowded region with an extremely rich variety of radio, IR, soft X-ray, GeV, and TeV sources. However, the *NuSTAR* view of the GC above $\sim$20 keV exhibits only two hard X-ray features—a point-like feature coincident with G359.95–0.04 and the CHXE (Figure 6). In the gamma-ray band, HESS detected a single source, HESS J1745–290 at R.A. $= 17^h45^m39^s\!.6$ and decl. $= -29°00'$ $22''$ (J2000) (Acero et al. 2010), that is spatially consistent with both Sgr A* and G359.95–0.04. In this section, we investigate a connection between the hard X-ray sources and the HESS source as well as their emission mechanisms, based on our spectral analysis results using *NuSTAR*, *XMM-Newton*, and *Chandra* data. A multi-wavelength SED analysis is discussed in the subsequent section to elucidate the TeV emission mechanisms.

7.1. Joint NuSTAR and XMM-Newton Spectral Analysis

We extracted *NuSTAR* spectra from a circular region of radius $40''$ around the *Chandra* position of G359.95–0.04 (Wang et al. 2006), at R.A. $= 17^h45^m39^s\!.80$ and decl.$= -29°$ $00'19''\!.9$ (J2000). This radius was chosen to maximize the significance of the highest-energy spectral bins and minimize contamination from diffuse thermal emission given the *NuSTAR* PSF (e.g., HPD $\sim 60''$). The *NuSTAR* background spectra were extracted from a region from the same detector chip but excluding Sgr A East, the "Plume" (Park et al. 2005), and the molecular clouds (Ponti et al. 2010). We extended the energy band for spectral fitting to 50 keV, above which the internal detector background dominates.

To better constrain the low-energy components of this spectrum, we used EPIC-PN data from the two *XMM-Newton* observations (ObsID: 0694640301 and 0694641101) carried out in 2012 for which Sgr A* was placed near the center of the FOV (See Table 1). X-ray spectroscopy with *XMM-Newton* EPIC instruments constrains the Galactic column density better than *NuSTAR* by fitting the spectrum below 3 keV, and it resolves Fe lines at 6.7 keV (He-like) and 6.9 keV (H-like), thus measuring the plasma temperature accurately. We extracted an *XMM-Newton* spectrum from the same region as used for the *NuSTAR* analysis. We generated response files and background spectra following the procedures described in Section 3.3. We used the 2–8 keV band for fitting the *XMM-Newton* spectra.

To fit the 2–50 keV spectrum of *XMM-Newton* and *NuSTAR*, we used the model `const * tbabs * (apec + apec + powerlaw + gauss)`. To account for the different overall normalization between *NuSTAR* and *XMM-Newton*, a constant relative normalization factor was allowed to vary. The
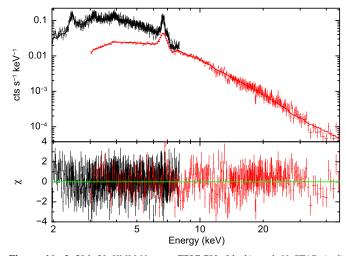

Figure 11. 2–50 keV *XMM-Newton* EPIC-PN (black) and *NuSTAR* (red) spectra of the central $r = 40''$ circular region around G359.95–0.04. The 2–8 keV spectrum is constructed from *XMM-Newton* EPIC-PN data, while the 3–50 keV spectrum is constructed from *NuSTAR* data. The model used is an absorbed two-temperature thermal plasma plus a power-law and a Gaussian line at 6.4 keV.

abundances of the two thermal components were fit freely within the range measured by the previous analysis (Baganoff et al. 2003; Sakano et al. 2004). The *NuSTAR* and *XMM-Newton* spectra of the central $40''$ region are shown in Figure 11 and the best-fit parameters are listed in Table 4. The lower-temperature component, at $kT = 1.2$ keV, corresponds to a combination of the thermal emission from stellar winds in the central $10''$ region (Baganoff et al. 2003) and the low-temperature component of Sgr A East (Sakano et al. 2004). The higher-temperature component, at $kT = 6.7$ keV, is consistent with the high-temperature component of Sgr A East in the region near Sgr A* (Sakano et al. 2004). The power-law component has a best-fit photon index $\Gamma = 0.152^{+0.19}_{-0.16}$ and a 20–40 keV flux of $F_X = (2.3 \pm 0.1) \times 10^{-12}$ erg cm^{-2} s^{-1}.

7.2. Can G359.95–0.04 and the CHXE Account for the 20–40 keV Emission in the Central 10 pc Region?

In order to assess the presence of a hard X-ray extension of G359.95–0.04 above 10 keV, we performed spatially resolved spectral analysis using the *Chandra* data. *Chandra* measured a photon index of $\Gamma = 1.94^{+0.17}_{-0.14}$ for G359.95–0.04, but with a spectral softening from the head to tail ranging from $\Gamma \sim 1.3$–3.0 (Wang et al. 2006). The high-energy spectrum of this object is then most accurately modeled as a summation of spectra with different photon indices rather than a simple extrapolation of the best-fit photon index. We refit the spectrum extracted from the same region used by Wang et al. (2006) using a more extensive set of *Chandra* data. This yields a photon index of $\Gamma = 1.8 \pm 0.1$, consistent with the previous measurements. We then divide the Wang et al. (2006) region into three sub-regions of equivalent areas, yielding $\Gamma_1 = 1.5 \pm 0.1$, $\Gamma_2 = 1.7 \pm 0.1$ and $\Gamma_3 = 2.6 \pm 0.1$, listed in order from the head toward the tail. Then, we constructed a composite spectral model for G359.95–0.04 from a set of *Chandra* fluxes and photon indices from the three segmented regions in the filament, and extrapolated it to the hard X-ray band. The composite model gives a 20–40 keV flux of $0.97^{+0.22}_{-0.09} \times 10^{-12}$ erg cm^{-2} s^{-1}.

Table 4
XMM-Newton and *NuSTAR* Spectral analysis Results of the Central
$r = 40''$ Region around G359.95–0.04

Parameters	Best-fit Values
N_H (10^{22} cm^{-2})	17 ± 3
kT_1 (keV)	1.17 ± 0.03
Abundance Z_1	$1.9^{+0.3}_{-0.2}$
$norm_1$	$(3.7 \pm 0.4) \times 10^{-2}$
kT_2 (keV)	6.7 ± 0.4
Abundance Z_2	$1.6^{+0.4}_{-0.2}$
$norm_2$	$4.5^{+0.4}_{-0.2} \times 10^{-3}$
Fe Kα equivalent width (eV)	26 ± 5
PL photon index (Γ)	$1.52^{+0.19}_{-0.16}$
PL flux (20–40 keV)[a]	$(2.3 \pm 0.1) \times 10^{-12}$
χ^2_ν [dof]	1.13 (846)

Notes. The energy band is 2–50 keV. The errors are 68% confidence level. The overall flux normalization between the *NuSTAR* and *XMM-Newton* spectra is 1.3 ± 0.1.
[a] The flux unit is 10^{-12} erg cm^{-2} s^{-1}.

Perez et al. (2015) showed the southwest and northeast region symmetrically located inside the CHXE ellipse have identical hard X-ray spectra, described equivalently well by either a power law with $\Gamma \approx 1.6$ or thermal bremsstrahlung with $kT \approx 55$ keV. By repeating the same spectral analysis with the latest *NuSTAR* pipeline version, we determined the 20–40 keV flux of 0.56×10^{-12} erg cm^{-2} s^{-1} in the southwest region of the CHXE. Using the spatial model of the CHXE presented in Section 4.2, we calculate the 20–40 keV flux of the CHXE to be $(1.08 \pm 0.14) \times 10^{-12}$ erg cm^{-2} s^{-1} in the central $40''$ region around Sgr A*, assuming that the CHXE has a power-law spectrum with $\Gamma = 1.6$ throughout its entire region.

The sum of the estimated G359.95–0.04 and CHXE flux ($2.1^{+0.5}_{-0.3} \times 10^{-12}$ erg cm^{-2} s^{-1}) matches with the observed 20–40 keV flux in the central $40''$ region ($2.3 \pm 0.1 \times 10^{-12}$ erg cm^{-2} s^{-1}) within the error bars. In addition, the spectral model consisting of a hard X-ray extension of G359.95–0.04 and the CHXE emission reproduces the 20–40 keV *NuSTAR* spectrum since the measured PL index of $\sim$1.5 is similar to those of G359.95–0.04 and the CHXE. This result confirms that 20–40 keV emission in the central $40''$ region is predominantly due to the CHXE and G359.95–0.04. Our imaging analysis in Section 4.3 shows G359.95–0.04 is more prominent above 40 keV likely because G359.95–0.04 has a slightly harder X-ray spectrum and is more compact than the CHXE. While other X-ray sources may contribute to the hard X-ray emission in the central $40''$ region, our error analysis indicates their contribution should be less than 2×10^{-13} erg cm^{-2} s^{-1} in the 20–40 keV band. This upper limit will be useful in constraining models of X-ray and particle emission in the central parsec region around Sgr A*.

7.3. Connection with the TeV Source HESS J1745–290

Our imaging and spectral analysis shows that above 20 keV hard X-ray emission in the central 10 pc region is composed of the CHXE and G359.95–0.04. No gamma-ray emission is expected from the CHXE since it is likely an unresolved population of massive magnetic CVs (Hailey et al. 2015), while only a rare subclass of HMXBs are known to emit TeV gamma-rays (Dubus 2013). Thus, it leaves only G359.95–0.04 as a hard X-ray counterpart candidate for HESS J1745–290.

Previously, any models proposing that leptons are emitted from Sgr A* or its vicinity within a few pc have had great difficulties with explaining the large extent of the diffuse hard X-ray source IGR J17456–2901 since the synchrotron cooling time of $\gtrsim$10 TeV electrons emitting hard X-ray photons is as short as $\sim$10 years (Neronov et al. 2005; Hinton & Aharonian 2007). Now that *NuSTAR* has revealed the compact hard X-ray emission above 40 keV is centered around G359.95–0.04, this "cooling time" problem associated with IGR J17456–2901 no longer exists.

In order to explore whether G359.95–0.04 alone can account for the GC TeV emission spectroscopically, we developed a one-zone PWN model following Zhang et al. (2008) and used it to fit the broadband SED data in the central parsec region. Our model inputs are PWN age, magnetic field strength at present, a broken power-law spectrum for electron injection [$F(E_e) \sim E_e^{-p1}$ at $E_e \leqslant E_{break}$ and E_e^{-p2} at $E_e > E_{break}$] with the lower and upper energy limits, the radiation density in the IR, optical and UV bands, as well as pulsar spin-down parameters. For the SED data, we adopt the X-ray spectrum of G359.95–0.04 from our *Chandra* and *NuSTAR* spectral analysis and the TeV spectrum of HESS J1745–290 from Aharonian et al. (2009). The radio non-detection with an upper limit of 5×10^{-17} erg cm^{-2} s^{-1} from 6 cm observations (Hinton & Aharonian 2007) is also taken into account in our analysis. Hereafter, we do not consider the *Fermi* GeV source 2FGL J1745.6–2858 at R.A. = $17^h45^m41\overset{s}{.}6$ and decl. = $-28°58'43''$ (J2000) since it lies outside the error circle of HESS J1745–290 (Nolan et al. 2012; Yusef-Zadeh et al. 2013). 2FGL J1745.6–2858 may well be associated with the aforementioned X-ray filament G359.97–0.038 (Nynka et al. 2015).

Figure 12 shows the best-fit SED model along with the radio, X-ray and TeV data. Following Hinton & Aharonian (2007), we assumed G359.95–0.04 is a 10^4 year-old PWN with a spin-down power of 5×10^{35} erg s^{-1} and its magnetic field strength is 300 μG at present. We find that these parameters fit the SED data reasonably well. In the central parsec region, the radiation density can be as high as $\sim$5 $\times$ 10^3 eV cm^{-3} (Davidson et al. 1992). We adopted the FIR, optical and UV radiation density from Hinton & Aharonian (2007) who quoted the original work of Davidson et al. (1992). We found that a broken power-law electron spectrum with $p_1 = 1.8$, $p_2 = 2.0$ and $E_{break} = 50$ TeV represents the shape of the X-ray and TeV spectrum well. These electron injection parameters are typical of young PWNe (Zhang et al. 2008). The maximum electron energy was set to 200 TeV to account for the energy cut-off at 4 TeV in the gamma-ray spectrum (Aharonian et al. 2009). A low energy cut-off at $E_e \gtrsim 0.5$ TeV was required so that the model is consistent with the non-detection of G359.95–0.04 in the radio band. Alternatively, Hinton & Aharonian (2007) proposed fast electron diffusion to account for the lack of a radio counterpart. Both the upper and lower limit in the electron injection spectrum are similar to those of Hinton & Aharonian (2007) who analyzed the same SED data except using the X-ray spectrum of the *INTEGRAL* source IGR J17456–2901. In conclusion, we find that G359.95–0.04 alone, likely a $\sim$10^4 year-old PWN with nominal electron injection parameters, can account for the broadband SED of the central parsec region including HESS J1745–290. It is
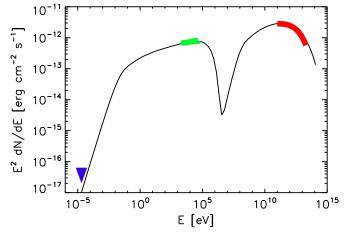
Figure 12. One-zone PWN model fit to the broad-band SED data including the 6 cm radio flux upper limit (blue arrow), G359.95–0.04 X-ray spectrum (green) and 0.1–10 TeV HESS spectrum of HESS J1745–290 (red).

noteworthy that the other distinct TeV gamma-ray source within a degree from the GC is associated with another young PWN in SNR G0.9+0.1 (Aharonian et al. 2005).

As an alternative leptonic scenario for the GC TeV emission, stellar wind shocks from massive stars in the central stellar cluster can efficiently accelerate electrons (Quataert & Loeb 2005), or Sgr A* itself can eject high-energy electrons (Kusunose & Takahara 2012). Due to the fast electron cooling time either by synchrotron radiation or inverse Compton scattering in the GC, hard X-ray emission should be localized around an electron acceleration site. While these emission mechanisms may be in action, our *NuSTAR* analysis indicates that their contribution is insignificant since the hard X-ray emission above 40 keV is spatially and spectroscopically consistent with G359.95–0.04. Therefore, the PWN candidate G359.95–0.04 seems to be the most plausible hard X-ray counterpart of the TeV source HESS J1745–290.

The hadronic scenario may be plausible as well based on the fact that diffuse TeV emission is spatially well correlated with molecular clouds in the GC (Aharonian et al. 2006). One potential source of ejecting high energy protons is Sgr A* (Aharonian et al. 2006; Ballantyne et al. 2007; Dogiel et al. 2009c; Ballantyne et al. 2011). Among a number of hadronic models proposed for the gamma-ray emission in the GC, there has been no specific prediction for X-ray spectra in the central parsec region. Rather, they have been focused on larger degree-size regions over which protons can propagate without losing kinetic energies significantly (Dogiel et al. 2009b). Similar to the LECR model, either non-thermal bremsstrahlang or synchrotron is expected to be the primary X-ray emission mechanism via secondary electrons produced by hadronic interactions between high energy protons and molecular clouds (Dogiel et al. 2009b, 2009c; Gabici et al. 2009). Such X-ray emission must be most prominent at the location of molecular clouds or high-density gas in the vicinity of Sgr A*, potentially with Fe Kα line emission at 6.4 keV (Dogiel et al. 2009a). In addition, X-ray emission in the hadronic scenario should have a larger extent than in the leptonic scenario since protons have significantly longer cooling times than electrons in the GC where both magnetic field and radiation density are high. To the contrary, hard X-ray emission above 40 keV is highly concentrated around G359.95–0.04, and *Chandra* did not detect strong Fe Kα emission within 10 pc around Sgr A*,

including the circumnuclear disk (Baganoff et al. 2003). Therefore, the hadronic scenario is unlikely to be a major contributor for the hard X-ray and TeV emission in the central parsec region.

8. SUMMARY

The initial 450 ks phase of the *NuSTAR* GC program, with its high-resolution imaging and spectroscopic capability from 3 to 79 keV, has made unique contributions to understanding high-energy phenomena in the crowded GC region as listed below.

1. *NuSTAR* resolved the *INTEGRAL* source IGR J17456–2901 into non-thermal X-ray filaments, molecular clouds, point sources and the previously unknown CHXE above 20 keV.
2. The X-ray emission from Sgr A East is thermal with $kT \sim 1$–6 keV with no evidence of non-thermal emission, and is consistent with the previous soft X-ray observations (Maeda et al. 2002; Sakano et al. 2004).
3. In the 20–40 keV band, *NuSTAR* discovered hard X-ray emission (CHXE) centered on Sgr A*. The CHXE is elongated along the Galactic Plane with an elliptical extent of ~8 pc (Galactic longitude) and ~4 pc (Galactic latitude) (Perez et al. 2015). The most likely explanation for the CHXE is an unresolved population of massive magnetic CVs (largely intermediate polars) with $M_{WD} \sim 0.9 \, M_{\odot}$ (Hailey et al. 2015).
4. *NuSTAR* detected four non-thermal X-ray filaments (G359.89–0.08, G359.97–0.038, G0.13–0.11 and G359.95–0.04) above 10 keV. The origin of non-thermal X-ray filaments may be heterogeneous and associated with different emission mechanisms such as magnetic flux tubes trapping TeV electrons (Zhang et al. 2014), SNR–cloud interaction and PWNe (Nynka et al. 2015).
5. For the first time, *NuSTAR* resolved hard X-ray emission from the Sgr A clouds above 10 keV and unambiguously detected hard X-ray continuum emission from MC1 and the Bridge. Hard X-ray continuum emission is spatially correlated with Fe Kα line emission (EW ~ 1 keV) from these clouds. We fit the Monte-Carlo based MYTorus model to the *XMM-Newton + NuSTAR* spectra of MC1 and the Bridge, and determined their intrinsic column densities ($N_{H} \sim 10^{23} \, cm^{-2}$) and the primary X-ray spectra with $\Gamma \sim 2$ self-consistently. We set a firm lower bound for X-ray luminosity of Sgr A* flares illuminating MC1 and the Bridge to $L_X \gtrsim 10^{38} \, erg \, s^{-1}$. It is still unclear whether the Sgr A and Sgr B clouds were illuminated by different Sgr A* flares in the past.
6. A point-like hard X-ray source observed in the 20–60 keV band is identified as the PWN candidate G359.95–0.04, 9″ away from Sgr A*. The hard X-ray emission in the central 10 pc region is predominantly composed of two sources, G359.95–0.04 and the CHXE.
7. In the central 10 pc around Sgr A*, G359.95–0.04 is the primary hard X-ray feature that is expected to emit TeV gamma-rays via inverse Compton scattering of IR, optical and UV photons. Our SED study suggests that G359.95–0.04 is the hard X-ray counterpart of the persistent TeV source HESS J1745–290, thus strongly favoring the leptonic origin of the TeV emission at the very center of our galaxy.

Follow-up deep observations by *NuSTAR* will lead to further spectral identification of X-ray filaments and point sources. Monitoring time variation of the GC molecular clouds jointly by *NuSTAR* and *XMM-Newton* will elucidate their X-ray emission mechanism and probe the primary illuminating source or Sgr A* flaring activity in the past. Starting from 2015 April, the *NuSTAR* Legacy program will follow up some of the hard X-ray sources discussed in this paper with deeper exposures.

APPENDIX
NuSTAR BACKGROUND IN THE GC OBSERVATION

NuSTAR imaging and spectral analysis of GC sources is challenging due to the high background level and to its complex multiple components. The *NuSTAR* background is generally characterized by four different components as outlined below. More detailed discussion on the CXB and internal background can be found in Wik et al. (2014).

1. Focused diffuse background (2-bounce background photons): diffuse background photons in the FOV are reflected twice by the optics and focused on the detector plane.
2. Ghost-rays (1-bounce background photons): Photons from outside the FOV are reflected once by the optics and reach the detector plane. Ghost-ray photons from a bright persistent source or X-ray transient can be significant, with a visible pattern in the *NuSTAR* image. Although some observations of the GC and Norma field have been severely affected by ghost-ray background (Bodaghee et al. 2014), it is not important in the *NuSTAR* mini-survey and Sgr A* observations.
3. Stray-light or aperture background (0-bounce background photons): Photons from any X-ray source at ~1°–5° away from the telescope pointing vector, that are not blocked by the aperture stop, illuminate the detector plane. SLB is not uniform over the detector plane, and it is not identical between the two focal plane modules. The location of SLB is sensitive to the position angle (PA) of the telescope.
4. Internal detector background (cosmic-ray induced background photons): atmospheric albedo and activation components with several emission lines in the 20–40 keV band. Above ~40 keV, this component usually becomes more important than the other background components.

Figure 13 shows example *NuSTAR* images (FPMA and FPMB images from ObsID: 40032010001) exhibiting both ghost-ray background and SLB. The radiating pattern in the lower-left corner of both the FPMA and FPMB image is due to the ghost-ray background photons from the bright persistent LMXB 1A1742–294 at R.A. = $17^h46^m05\overset{s}{.}201$ and decl. = $-29°30'53\overset{''}{.}3$ (J2000) (Wijnands et al. 2006). On the other hand, the bright region in the upper-left corner of the FPMA image is due to the SLB from the bright X-ray source GX 3+1 (Seifina & Titarchuk 2012).

A.1. SLB Removal from Bright X-Ray Point Sources

In some observations, SLB from a point source brighter than $\sim 10^{-11}$ erg cm^{-2} s^{-1} can be easily visible in raw *NuSTAR* images (Figure 13). For a given PA and a list of nearby bright point sources, we can exactly predict the SLB pattern on the detector plane. Using a code developed specifically for calculating the SLB pattern from a point source with known position, we can generate a bad-pixel map for each detector module and observation, and then filter out events and exclude exposure map in regions of high SLB. This is one of the *NuSTAR* data filtering processes discussed in Section 2, before proceeding to further imaging and spectral analysis.

A.2. Background Spectrum Subtraction

For all GC sources discussed in this paper, the primary background component below ~40 keV is focused diffuse background and SLB, while the instrumental background dominates above ~40 keV. For example, Figure 14 shows a *NuSTAR* background spectrum extracted from a region free from point sources and molecular clouds in one of the *NuSTAR* mini-survey observations (ObsID 40032001002). As shown in Figure 14, SLB from the Galactic Ridge X-ray emission (sGRXE) is usually dominant over that of cosmic X-ray background (sCXB). This background spectrum is typical to *NuSTAR* GC observations. Focused CXB and GRXE components are not shown in the figure since their fluxes are lower than their stray-light components by an order of magnitude. Both the CXB and internal background are modeled by the *nulyses* or *nuskybkg* software package using the high-latitude *NuSTAR* data (Wik et al. 2014). The sGRXE spectrum is well represented by an absorbed thermal spectrum (APEC model in XSPEC) with $kT \sim 12$ keV and an Fe Kα emission line at 6.4 keV.

The background count rate per detector area [cm^{-2}] extracted from relatively source-free regions in the *NuSTAR* mini-survey observations varies between 2.1×10^{-2} and 6.3×10^{-2} cts s^{-1} cm^{-2} in the 3–20 keV band. After subtracting the model count rates from the sCXB component and internal detector background (Wik et al. 2014), the 3–20 keV
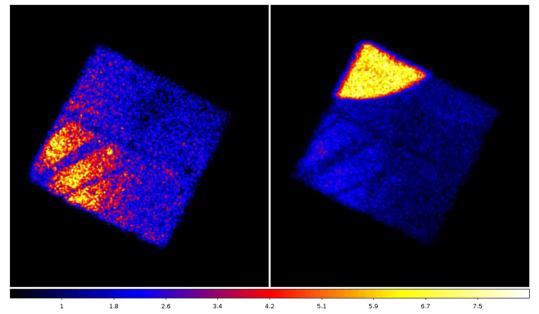
Figure 13. *NuSTAR* FPMA (left) and FPMB (right) image in the sky coordinates from *NuSTAR* observation 40032010001 pointing at R.A. = 266°.0754 and decl. = −29°.2988 (J2000), with PA = 332°.
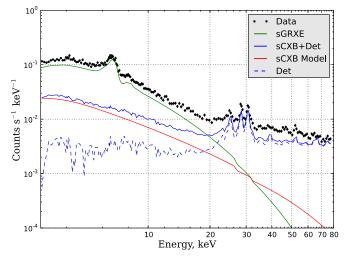

Figure 14. *NuSTAR* background spectrum taken from a region (ObsID: 40032001002) where there is no known X-ray source, overlaid with the CXB components and internal background.

a source spectrum from another nearby observation with a similar PA (off-source background subtraction; Krivonos et al. 2014). For instance, the Sgr A complex has significant GC thermal emission so the former conventional background subtraction should be applied. On the other hand, the off-source background subtraction is more appropriate for the Arches cluster where the SLB is more significant than the focused GC diffuse emission (Krivonos et al. 2014).

While the sCXB component can be accurately modeled using *NuSTAR* extragalactic deep survey data (Wik et al. 2014), there is no reliable background model for the sGRXE component due to the complex and unknown spatial distribution of the GRXE. Instead, as guidance, we used the sGRXE count rates determined from the *NuSTAR* mini-survey data to estimate whether the sGRXE is dominant over other background components for a given source region. For some sources, the situation is "mixed" where both the focused diffuse background and SLB have similar count rates. In this case, we applied both background subtraction methods to bound the problem.

sGRXE count rate ranges from 1.4×10^{-2} (ObsID: 40010003001) to 5.5×10^{-2} cts s^{-1} cm^{-2} (ObsID: 40010001002) with the mean count rate of 4×10^{-2} cts s^{-1} cm^{-2}. The sGRXE component accounts for ∼70%–90% of the total background count rate in the 3–20 keV band. Both sGRXE count rate and its fraction to the overall background varies between different observations, PA and detector modules.

The relative significance between the focused diffuse background and the SLB varies between different regions in the *NuSTAR* image. When focused diffuse emission is dominant, one can extract a background spectrum from a region away from the source on the same detector chip over which the instrumental background is uniform (Harrison et al. 2013). When SLB is dominant, we extract a background spectrum using the same *detector* region used for extracting

A.3. Comparison of X-Ray Reflection Models applied to GC Molecular Clouds

In general, the X-ray reflection spectrum from a GC cloud is composed of scattered continuum, Fe fluorescent lines and photo-absorption edges. A popular XRN model for GCMCs is an absorbed power-law continuum with two Gaussian emission lines for the Fe Kα and Kβ lines respectively: `tbabs` `*` `(powerlaw + gauss + gauss)` where `tbabs` model, sometimes replaced by `wabs`, represents intrinsic absorption in the cloud. This model assumes that Fe fluorescent photons come from the center of a cloud, while another form `tbabs*powerlaw + gauss + gauss` assumes that Fe fluorescent photons come from the surface and are therefore not subject to photo-absorption in the cloud. In practice, there is almost no difference between these two cases unless the cloud column density is extremely high. However, this ad hoc

XRN model lacks self-consistency since photo-absorption, scattered continuum and fluorescent lines are decoupled and fit separately. The scattered continuum is represented by a single power-law model assuming that the primary X-ray spectrum shape is unperturbed by Compton scattering. This assumtion is valid only for low energy photons where Compton scattering is negligible, and when a cloud is optically thin ($N_H \ll 10^{24}\,cm^{-2}$).

In the other extreme case, slab geometry models such as `pexrav`, `pexmon` and `reflionx` calculate X-ray reflection spectra self-consistently from a slab with infinite optical depth (Magdziarz & Zdziarski 1995; Ross & Fabian 2005; Nandra et al. 2007). Ponti et al. (2010) applied the `pexrav` model to Sgr A molecular clouds, while `reflionx` has been used to fit X-ray spectra of the Arches cluster (Krivonos et al. 2014) and the Sgr B2 cloud (Zhang et al. 2015). However, the major drawback of these slab geometry models is that they are applicable only for Compton-thick clouds ($\tau_T \gg 1$ or $N_H \gg 10^{24}\,cm^{-2}$), and they do not allow for a measurement of the column density. Both our spectral analysis and independent N_H measurements suggest that the Sgr A clouds are optically thin with $N_H \sim 10^{23}\,cm^{-2}$.

None of the above models can determine the intrinsic column density of a cloud and the primary X-ray spectrum self-consistently. As demonstrated by recent X-ray studies of Compton-thick AGN, Monte-Carlo simulation is the only viable approach to build a self-consistent X-ray reflection model (Murphy & Yaqoob 2009). In the past, Sunyaev & Churazov (1998), Revnivtsev et al. (2004) and Odaka et al. (2011) studied X-ray morphology and spectra of GCMCs using Monte-Carlo based X-ray reflection models. These models explored some limited parameter space primarily for Sgr B2, but they are not implemented in XSPEC for spectral fitting. At present, the MYTorus model is the only X-ray reflection model that is available in XSPEC that can measure the intrinsic column density self-consistently for GCMCs (Murphy & Yaqoob 2009; Yaqoob 2012). The MYTorus model employs Monte-Carlo simulation of reprocessing X-ray photons from a toroidal reprocessor, and it enables "real-time" spectral fitting in XSPEC using tabulated Green's function data. The other X-ray reflection models available in XSPEC either assume infinite column density or do not separate a reflected component (Brightman & Nandra 2011). Although the MYTorus model was originally developed to study Compton-thick AGNs with a toroidal X-ray reflector, we find that it is applicable to X-ray spectral analysis of GCMC data with some restrictions as shown in the next section. Table 5 compares the three XRN models used in our analysis, their assumptions, limitations and valid parameter ranges.

A.4. Applicability of MYTorus Model to X-Ray Spectroscopy of GC Molecular Clouds

Since the MYTorus model was developed primarily for studying X-ray reflection spectra of Compton-thick AGN, it assumes a torus with completely neutral material and uniform density (Murphy & Yaqoob 2009). The MYTorus model covers a range of the equatorial column density $N_H = 10^{22}$–$10^{25}\,cm^{-2}$ and power-law photon indices $\Gamma = 1.4$–2.6. Note that the MYTorus model defines the inclination angle between an observer's LOS and the symmetry axis of the torus (θ_{obs}), while most publications on GCMCs use a scattering angle (θ) of illuminating photons off the cloud to the observer (Capelli

et al. 2012). See Figure 15 for the geometry of a cloud and the torus as well as the definition of the incident and scattering angle. A face-on viewing case for the MYTorus model ($\theta_{obs} = 0°$) corresponds to the scattering angle $\theta = 90°$ when a cloud is in the same projected plane as the primary X-ray source. For each of the three key assumptions associated with the MYTorus model, below we investigate the valid parameter space where the model is applicable to analyze X-ray reflection spectra of molecular clouds in general.

1. The reflector geometry is toroidal.

　　We explored a large range of θ_{obs} and N_H to investigate the validity of MYTorus model application to a quasi-spherical cloud. To begin with, a face-on case ($\theta_{obs} = 0°$) provides an accurate solution for a cloud since the axial symmetry is preserved for X-ray photon reflection with respect to a distant observer. We can obtain reflected X-ray flux from the cloud (which is a part of the virtual torus, i.e., the red circle in Figure 15) by scaling the best-fit primary X-ray flux by a solid angle ratio of the torus (fixed to $\Omega/4\pi = 0.5$) and the cloud. In this way, we "collect" X-rays reflected from the cloud only and "abandon" X-rays reflected from the rest of the torus (the gray area in Figure 15). N_H and Γ remain the same regardless of the cloud geometry. As θ_{obs} deviates from the face-on case, different azimuthal parts around the torus can scatter X-rays at different angles therefore the MYTorus model spectrum may show some variation with the inclination angle θ_{obs} and become inaccurate for a quasi-spherical cloud.

　　However, we find that the scattered continuum component (MYTS) does not vary with θ_{obs} strongly as long as $\theta_{obs} \lesssim 60°$ and the cloud is optically thin ($N_H \lesssim 10^{24}\,cm^{-2}$). Figure 16 shows MYTS model spectra at various inclination angles for $N_H = 10^{23}$ and $10^{24}\,cm^{-2}$. There are two reasons for the strong angular dependence at $\theta_{obs} \gtrsim 60°$. First, since the half-opening angle of the torus is fixed to $60°$, some back-scattered X-ray photons from one side of the torus can hit the other side thus they are subject to further absorption before reaching an observer at $\theta_{obs} \geqslant 60°$. This is peculiar to the assumed torus geometry of the MYTorus model. Second, multiple scattering can induce some angular dependence of X-ray reflection spectra but it is negligible at $N_H \lesssim 10^{24}\,cm^{-2}$. Odaka et al. (2011), who simulated X-ray reflection spectra for the Sgr B2 cloud (with a spherical shape assumed), found that the scattered X-ray continuum spectrum and morphology do not depend on the location of the cloud and incident angle significantly when the cloud is not Compton thick. Moreover, the scattered X-ray flux is proportional to the total mass (or solid angle for a given N_H) of a cloud regardless of its shape, if it is optically thin (Cramphorn & Sunyaev 2002).

　　To quantify the (in)sensitivity to θ_{obs} or assumed geometry, we made simulated MYTS spectra for $\theta_{obs} = 60°$ at $N_H = 10^{23}$–$10^{25}\,cm^{-2}$, then we fit the simulated spectra with the MYTS model with θ_{obs} fixed at $0°$. We measured the deviation of N_H, Γ and normalization from their input values, and adopted them as systematic errors associated with the MYTorus model. At $N_H = 10^{23}\,cm^{-2}$, N_H, Γ and normalization deviate from the input values by $\sim$10%, 1% and 7%, respectively. At

Table 5
Comparison of three X-Ray Reflection Spectral Models applied to GC Molecular Clouds

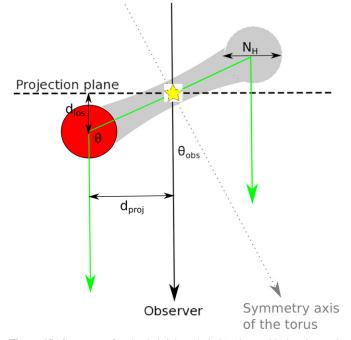| Model	Ad hoc XRN	Slab geometry	MYTorus
Geometry	undefined	semi-infinite slab	torus
XSPEC model	`tbabs*(powerlaw + gauss + gauss)`	`pexrav`, `pexmon`, `reflionx`	`MYTS + MYTL`
Column density	absorption only	infinite column density	self-consistent measurement
Primary X-ray PL index	same as the best-fit PL index	model output	model output
Primary X-ray source flux	adjustment by Thomson depth	model output scaled by solid angle	model output scaled by solid angle
Fe abundance	unspecified	variable	fixed to solar
Valid parameter range	no self-consistency	only for optically thick cloud	$\theta_{\rm obs} \lesssim 60°$ and $N_{\rm H} \lesssim 10^{24}\,{\rm cm}^{-2}$

Figure 15. Geometry of a cloud (bright red circle) along with the observer's LOS (solid vertical line) and the projection plane (dashed horizontal line) of the X-ray source (yellow star). $d_{\rm proj}$ is the projected distance between the cloud and the source seen by the observer at the bottom, while $d_{\rm los}$ is the LOS distance of the cloud measured from the projection plane. A virtual torus for the MYTorus model is indicated by gray area. The inclination angle $\theta_{\rm obs}$ is between the observer's LOS and the symmetry axis of the torus (dotted gray line). The equatorial column density $N_{\rm H}$ is defined over the minor diameter of the torus. Photons from the X-ray source are scattered off the cloud into the observer's LOS at an angle θ (X-ray photon's paths are indicated by green lines). $\theta_{\rm obs} = 0°$ (face-on view) corresponds to $\theta = 90°$ ($d_{\rm los} = 0$) where the cloud is in the projection plane of the X-ray source.

$N_{\rm H} = 10^{24}\,{\rm cm}^{-2}$, the deviation increases to $\sim 25\%$, 3% and 10%.

We also compared an absorbed power-law model (`tbabs*powerlaw`) with the MYTorus model spectra in Figure 16. We adopted the mean column density of $(\pi/4)N_{\rm H}$ over all LOS through the torus (Murphy & Yaqoob 2009), power-law index of $\Gamma = 2$ and flux normalization roughly adjusted to the MYTorus model spectra in high energy band where photo-absorption is negligible. Note that the ad hoc XRN models predict significantly lower X-ray fluxes than the MYTorus models in low energy band. This is due to the fact that the ad hoc XRN model uses a single absorption term with a charateristic column density whereas photo-absorption takes place in various locations in the cloud with different optical depths. Based on simulation, we

find that the ad hoc XRN model yields a column density lower than the equatorial column density ($N_{\rm H}$) from the MYTorus model by a factor of ~ 2–3 in the range of $N_{\rm H} = 10^{23}$–$10^{24}\,{\rm cm}^{-2}$.

Our primary goal is to determine the primary X-ray spectrum (e.g., Sgr A* flares) therefore we set $N_{\rm H} \lesssim 10^{24}\,{\rm cm}^{-2}$ as a valid range of MYTorus model application to molecular clouds because otherwise the systematic errors for Γ and normalization become larger than our statistical errors. We conclude that the reflected X-ray spectrum model in the *NuSTAR* energy band (3–79 keV) is not sensitive to the geometry of a reflector as long as $\theta_{\rm obs} \lesssim 60°$ and $N_{\rm H} \lesssim 10^{24}\,{\rm cm}^{-2}$. In this range, similarly to the face-on case, the incident X-ray flux for a given cloud can be obtained by scaling the best-fit X-ray flux from the MYTorus fit by the solid angle ratio of a cloud (typically $\Omega/4\pi \sim 10^{-2}$ for GCMCs) and the torus of the MYTorus model ($\Omega/4\pi = 0.5$) with $\lesssim 10\%$ errors. The best-fit power-law index from the MYTorus model fit can be adopted as that of the primary X-ray source with $\lesssim 3\%$ errors. On the other hand, a relation between $\theta_{\rm obs}$ and LOS distance of a cloud as well as its systematic errors cannot be well established. A modified version of the MYTorus model for more realistic cloud geometry (e.g., sphere) is under development and it will be used to determine the location of the GC molecular clouds and their primary X-ray source spectra more precisely without the restrictions described above.

2. The torus density profile is uniform.

Since we extract X-ray spectra from the entire cloud and collect all X-ray photons reflected toward us, we assume that any effects due to the non-uniformity of the density profile will be negligible at $N_{\rm H} \lesssim 10^{24}\,{\rm cm}^{-2}$ as multiple scattering is insignificant at these column densities. Also, the reflected X-ray flux is proportional to the total mass of a cloud if it is optically thin (Cramphorn & Sunyaev 2002). Thus, the primary X-ray flux will not be affected by different density profiles. It is, however, more important to take into account non-uniform density profile for X-ray morphology studies of GCMCs (Sunyaev & Churazov 1998; Odaka et al. 2011).

3. Fe abundance is fixed to solar.

Non-solar Fe abundance primarily affects Fe fluorescent lines at 6.4 and 7.0 keV and the Fe K absorption edge at 7.1 keV. While an unknown Fe abundance adds some uncertainty when one attempts to determine the primary X-ray luminosity solely from the Fe Kα line EW, broadband X-ray spectroscopy with *NuSTAR* extends to $E \gtrsim 10$ keV where the contribution of Compton scattering dominates over that of Fe fluorescent lines or photo-absorption. We confirmed that the fit parameters did not
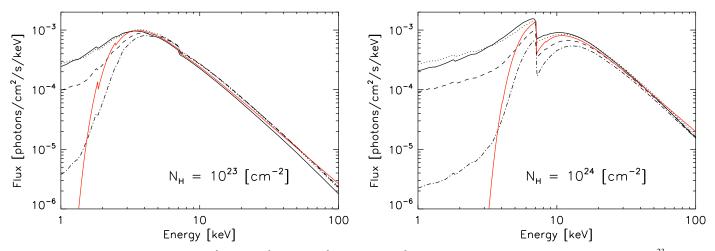
Figure 16. MYTorus model spectra at $\theta_{obs} = 0°$ (solid), $60°$ (dotted), $75°$ (dashed) and $90°$ (dot–dashed) for the equatorial column density $N_H = 10^{23}$ (left) and 10^{24} cm^{-2} (right). In all cases, we assumed an input power-law spectrum with $\Gamma = 2$. We used the same flux normalization for all the MYTorus model spectra. Note that the model spectra show strong angular dependence at $\theta_{obs} > 60°$ below ~ 3 keV ($N_H = 10^{23}$ cm^{-2}) and ~ 10 keV ($N_H = 10^{24}$ cm^{-2}). For comparison, we plot an absorbed power-law model (tbabs*powerlaw, red solid lines) with the mean column density of $(\pi/4)N_H$ over all lines-of-sight through the torus (Murphy & Yaqoob 2009), power-law index of $\Gamma = 2$ and flux normalization roughly adjusted to the MYTorus model spectra in high energy band.

vary significantly when we fit the MYTS (scattered continuum) model only to the *XMM-Newton + NuSTAR* spectra of MC1 and the Bridge without 6–10 keV energy bins where the Fe fluorescent lines and the K-edge are prominent. A new self-consistent XRN model based on the MYTorus model will implement data tables for different Fe abundances in the range of $Z_{Fe} = 0.5$–3 (T. Yaqoob 2015, private communication).

REFERENCES

Acero, F., Aharonian, F., Akhperjanian, A. G., et al. 2010, MNRAS, 402, 1877
Aharonian, F., Akhperjanian, A. G., Anton, G., et al. 2009, A&A, 503, 817
Aharonian, F., Akhperjanian, A. G., Aye, K.-M., et al. 2004, A&A, 425, L13
Aharonian, F., Akhperjanian, A. G., Aye, K.-M., et al. 2005, A&A, 432, L25
Aharonian, F., Akhperjanian, A. G., Bazer-Bachi, A. R., et al. 2006, Natur, 439, 695
Aharonian, F., & Neronov, A. 2005, Ap&SS, 300, 255
Albert, J., Aliu, E., Anderhub, H., et al. 2006, ApJL, 638, L101
Amo-Baladrón, M. A., Martín-Pintado, J., Morris, M. R., Muno, M. P., & Rodríguez-Fernández, N. J. 2009, ApJ, 694, 943
Archer, A., Barnacka, A., Beilicke, M., et al. 2014, ApJ, 790, 149
Arnaud, K. A. 1996, in ASP Conf. Ser. 101, Astronomical Data Analysis Software and Systems, ed. G. H. Jacoby & J. Barnes (San Francisco, CA: ASP), 17
Baganoff, F. K., Bautz, M. W., Brandt, W. N., et al. 2001, Natur, 413, 45
Baganoff, F. K., Maeda, Y., Morris, M., et al. 2003, ApJ, 591, 891
Ballantyne, D. R., Melia, F., Liu, S., & Crocker, R. M. 2007, ApJL, 657, L13
Ballantyne, D. R., Schumann, M., & Ford, B. 2011, MNRAS, 410, 1521
Bamba, A., Anada, T., Dotani, T., et al. 2010, ApJL, 719, L116
Barrière, N. M., Krivonos, R., Tomsick, J. A., et al. 2015, ApJ, 799, 123
Barrière, N. M., Tomsick, J. A., Baganoff, F. K., et al. 2014, ApJ, 786, 46
Bélanger, G., Goldwurm, A., Renaud, M., et al. 2006, ApJ, 636, 275
Bodaghee, A., Tomsick, J. A., Krivonos, R., et al. 2014, ApJ, 791, 68
Branduardi, G., Ives, J. C., Sanford, P. W., Brinkman, A. C., & Maraschi, L. 1976, MNRAS, 175, 47P
Brightman, M., & Nandra, K. 2011, MNRAS, 413, 1206
Bykov, A. M., Bocchino, F., & Pavlov, G. G. 2005, ApJL, 624, L41
Bykov, A. M., Chevalier, R. A., Ellison, D. C., & Uvarov, Y. A. 2000, ApJ, 538, 203
Capelli, R., Warwick, R. S., Porquet, D., Gillessen, S., & Predehl, P. 2012, A&A, 545, A35
Cembranos, J. A. R., Gammaldi, V., & Maroto, A. L. 2013, JCAP, 4, 51
Chen, W., Shrader, C. R., & Livio, M. 1997, ApJ, 491, 312

Chernyakova, M., Malyshev, D., Aharonian, F. A., Crocker, R. M., & Jones, D. I. 2011, ApJ, 726, 60
Christopher, M. H., Scoville, N. Z., Stolovy, S. R., & Yun, M. S. 2005, ApJ, 622, 346
Clavel, M., Terrier, R., Goldwurm, A., et al. 2013, A&A, 558, A32
Cramphorn, C. K., & Sunyaev, R. A. 2002, A&A, 389, 252
Davidson, J. A., Werner, M. W., Wu, X., et al. 1992, ApJ, 387, 189
Degenaar, N., Miller, J. M., Kennea, J., et al. 2013, ApJ, 769, 155
Degenaar, N., Wijnands, R., Cackett, E. M., et al. 2012, A&A, 545, A49
Dogiel, V., Cheng, K.-S., Chernyshov, D., et al. 2009a, PASJ, 61, 901
Dogiel, V. A., Chernyshov, D., Yuasa, T., et al. 2009b, PASJ, 61, 1093
Dogiel, V. A., Chernyshov, D. O., Yuasa, T., et al. 2009c, PASJ, 61, 1099
Dubus, G. 2013, A&ARv, 21, 64
Etxaluze, M., Goicoechea, J. R., Cernicharo, J., et al. 2013, A&A, 556, A137
Fender, R., & Belloni, T. 2004, ARA&A, 42, 317
Ferrière, K. 2009, A&A, 505, 1183
Freeman, P., Doe, S., & Siemiginowska, A. 2001, Proc. SPIE, 4477, 76
Gabici, S., Aharonian, F. A., & Casanova, S. 2009, MNRAS, 396, 1629
Gehrels, N., Chincarini, G., Giommi, P., et al. 2004, ApJ, 611, 1005
Hailey, C., Mori, K., Perez, K., et al. 2015, ApJ, submitted
Handa, T., Sakano, M., Naito, S., Hiramatsu, M., & Tsuboi, M. 2006, ApJ, 636, 261
Harrison, F. A., Craig, W. W., Christensen, F. E., et al. 2013, ApJ, 770, 103
Heard, V., & Warwick, R. S. 2013, MNRAS, 428, 3462
Hinton, J. A., & Aharonian, F. A. 2007, ApJ, 657, 302
Hong, J., Mori, K., Hailey, C. J., et al. 2015, ApJ, submitted
Inui, T., Koyama, K., Matsumoto, H., & Tsuru, T. G. 2009, PASJ, 61, 241
Johnson, S. P., Dong, H., & Wang, Q. D. 2009, MNRAS, 399, 1429
Jones, P. A., Burton, M. G., Cunningham, M. R., et al. 2012, MNRAS, 419, 2961
Kashyap, V. L., van Dyk, D. A., Connors, A., et al. 2010, ApJ, 719, 900
Kaspi, V. M., Archibald, R. F., Bhalerao, V., et al. 2014, ApJ, 786, 84
Koch, E. W., Bahramian, A., Heinke, C. O., et al. 2014, MNRAS, 442, 372
Koyama, K., Awaki, H., Kunieda, H., Takano, S., & Tawara, Y. 1989, Natur, 339, 603
Koyama, K., Hyodo, Y., Inui, T., et al. 2007, PASJ, 59, 245
Koyama, K., Maeda, Y., Sonobe, T., et al. 1996, PASJ, 48, 249
Krivonos, R., Revnivtsev, M., Churazov, E., et al. 2007, A&A, 463, 957
Krivonos, R. A., Tomsick, J. A., Bauer, F. E., et al. 2014, ApJ, 781, 107
Kusunose, M., & Takahara, F. 2012, ApJ, 748, 34
Li, Z., Morris, M. R., & Baganoff, F. K. 2013, ApJ, 779, 154
Linden, T., Hooper, D., & Yusef-Zadeh, F. 2011, ApJ, 741, 95
Lotti, S., Natalucci, L., Baganoff, F. K., et al. 2015, ApJ, submitted
Lu, F. J., Wang, Q. D., & Lang, C. C. 2003, AJ, 126, 319
Lu, F. J., Yuan, T. T., & Lou, Y.-Q. 2008, ApJ, 673, 915
Madsen, K. K., Harrison, F. A., Markwardt, C., et al. 2015, ApJ, 220, 8
Maeda, Y., Baganoff, F. K., Feigelson, E. D., et al. 2002, ApJ, 570, 671
Magdziarz, P., & Zdziarski, A. A. 1995, MNRAS, 273, 837

Mori, K., Gotthelf, E. V., Zhang, S., et al. 2013, ApJL, 770, L23
Morris, M., & Serabyn, E. 1996, ARA&A, 34, 645
Muno, M. P., Baganoff, F. K., Bautz, M. W., et al. 2004, ApJ, 613, 326
Muno, M. P., Baganoff, F. K., Brandt, W. N., Morris, M. R., & Starck, J.-L. 2008, ApJ, 673, 251
Muno, M. P., Baganoff, F. K., Brandt, W. N., Park, S., & Morris, M. R. 2007, ApJL, 656, L69
Muno, M. P., Bauer, F. E., Baganoff, F. K., et al. 2009, ApJS, 181, 110
Muno, M. P., Pfahl, E., Baganoff, F. K., et al. 2005, ApJL, 622, L113
Murakami, H., Koyama, K., & Maeda, Y. 2001, ApJ, 558, 687
Murphy, K. D., & Yaqoob, T. 2009, MNRAS, 397, 1549
Nandra, K., O'Neill, P. M., George, I. M., & Reeves, J. N. 2007, MNRAS, 382, 194
Neilsen, J., Nowak, M. A., Gammie, C., et al. 2013, ApJ, 774, 42
Neronov, A., Chernyakova, M., Courvoisier, T. J.-L., & Walter, R. 2005, arXiv:astro-ph/0506437
Nobukawa, M., Ryu, S. G., Tsuru, T. G., & Koyama, K. 2011, ApJL, 739, L52
Nolan, P. L., Abdo, A. A., Ackermann, M., et al. 2012, ApJS, 199, 31
Nowak, M. A., Neilsen, J., Markoff, S. B., et al. 2012, ApJ, 759, 95
Nynka, M., Hailey, C. J., Mori, K., et al. 2013, ApJL, 778, L31
Nynka, M., Hailey, C. J., Reynolds, S. P., et al. 2015, ApJ, 800, 119
Odaka, H., Aharonian, F., Watanabe, S., et al. 2011, ApJ, 740, 103
Park, S., Muno, M. P., Baganoff, F. K., et al. 2005, ApJ, 631, 964
Perez, K., Hailey, C. J., Bauer, F. E., et al. 2015, Natur, 520, 646
Ponti, G., Morris, M. R., Clavel, M., et al. 2014, in IAU Symp. 303, The Galactic Center: Feeding and Feedback in a Normal Galactic Nucleus, ed. L. O. Sjouwerman, C. C. Lang, & J. Ott (Cambridge: Cambridge Univ. Press), 333
Ponti, G., Morris, M. R., Terrier, R., & Goldwurm, A. 2013, in Advances in Solid State Physics, Vol. 34, ed. D. F. Torres & O. Reimer (Berlin: Springer-Verlag), 331
Ponti, G., Terrier, R., Goldwurm, A., Belanger, G., & Trap, G. 2010, ApJ, 714, 732
Quataert, E., & Loeb, A. 2005, ApJL, 635, L45
Reeves, J. N., & Turner, M. J. L. 2000, MNRAS, 316, 234
Reid, M. J. 1993, ARA&A, 31, 345
Reid, M. J., Menten, K. M., Zheng, X. W., Brunthaler, A., & Xu, Y. 2009, ApJ, 705, 1548
Reid, M. J., Readhead, A. C. S., Vermeulen, R. C., & Treuhaft, R. N. 1999, ApJ, 524, 816
Revnivtsev, M., Sazonov, S., Churazov, E., et al. 2009, Natur, 458, 1142

Revnivtsev, M., Sazonov, S., Gilfanov, M., Churazov, E., & Sunyaev, R. 2006, A&A, 452, 169
Revnivtsev, M. G., Churazov, E. M., Sazonov, S. Y., et al. 2004, A&A, 425, L49
Ross, R. R., & Fabian, A. C. 2005, MNRAS, 358, 211
Sakano, M., Warwick, R. S., Decourchelle, A., & Predehl, P. 2003, MNRAS, 430, 747
Sakano, M., Warwick, R. S., Decourchelle, A., & Predehl, P. 2004, MNRAS, 350, 129
Seifina, E., & Titarchuk, L. 2012, ApJ, 747, 99
Sunyaev, R., & Churazov, E. 1998, MNRAS, 297, 1279
Sunyaev, R. A., Markevitch, M., & Pavlinsky, M. 1993, ApJ, 407, 606
Tatischeff, V., Decourchelle, A., & Maurin, G. 2012, A&A, 546, A88
Terrier, R., Ponti, G., Bélanger, G., et al. 2010, ApJ, 719, 143
Tsuboi, M., Handa, T., & Ukita, N. 1999, ApJS, 120, 1
Tsuboi, M., Okumura, S. K., & Miyazaki, A. 2006, JPhCS, 54, 16
Tsuchiya, K., Enomoto, R., Ksenofontov, L. T., et al. 2004, ApJL, 606, L115
Verner, D. A., Ferland, G. J., Korista, K. T., & Yakovlev, D. G. 1996, ApJ, 465, 487
Wang, Q. D., Gotthelf, E. V., & Lang, C. C. 2002a, Natur, 415, 148
Wang, Q. D., Lu, F., & Lang, C. C. 2002b, ApJ, 581, 1148
Wang, Q. D., Lu, F. J., & Gotthelf, E. V. 2006, MNRAS, 367, 937
Weisskopf, M. C., Wu, K., Trimble, V., et al. 2007, ApJ, 657, 1026
Wijnands, R., in't Zand, J. J. M., Rupen, M., et al. 2006, A&A, 449, 1117
Wik, D. R., Hornstrup, A., Molendi, S., et al. 2014, ApJ, 792, 48
Wilms, J., Allen, A., & McCray, R. 2000, ApJ, 542, 914
Winkler, C., Courvoisier, T. J.-L., Cocco, G. D., et al. 2003, A&A, 411, L1
Worrall, D. M., Marshall, F. E., Boldt, E. A., & Swank, J. H. 1982, ApJ, 255, 111
Yaqoob, T. 2012, MNRAS, 423, 3360
Yuasa, T., Makishima, K., & Nakazawa, K. 2012, ApJ, 753, 129
Yusef-Zadeh, F., Arendt, R., Bushouse, H., et al. 2012, ApJL, 758, L11
Yusef-Zadeh, F., Hewitt, J. W., Wardle, M., et al. 2013, ApJ, 762, 33
Yusef-Zadeh, F., Law, C., & Wardle, M. 2002a, ApJL, 568, L121
Yusef-Zadeh, F., Law, C., Wardle, M., et al. 2002b, ApJ, 570, 665
Yusef-Zadeh, F., & Morris, M. 1987, ApJ, 322, 721
Yusef-Zadeh, F., Muno, M., Wardle, M., & Lis, D. C. 2007, ApJ, 656, 847
Zhang, L., Chen, S. B., & Fang, J. 2008, ApJ, 676, 1210
Zhang, S., Hailey, C. J., Baganoff, F. K., et al. 2014, ApJ, 784, 6
Zhang, S., Hailey, C. J., Baganoff, F. K., et al. 2015, ApJ, in press (arXiv:1507.08740)